Simplified Seismic Assessment of Buildings using Non-uniform Timoshenko Beam Model in Low-to-moderate Seismicity Regions

R.K.L. Su*,[1] and T.O. Tang[1] and K.C. Liu[1]

[1] *Department of Civil Engineering, The University of Hong Kong, Pokfulam Road, Hong Kong, PRC*

Abstract

In low-to-moderate seismicity regions, the limited seismic displacement demands could probably render tall buildings remaining nearly elastic during a maximum considered earthquake. Previous studies have shown the capability of the uniform Timoshenko beam model in resembling the dynamic behaviors of regular buildings. This article describes response spectrum analyses on the non-uniform Timoshenko beam model, considering the first four vibration modes to assess the seismic demands on various building types, which encompass low-rise wall or frame buildings and high-rise shear wall buildings with or without transfer structures. Simplified design charts correlating the global seismic demands – spectral accelerations, maximum interstory drift ratios, roof drift ratios and required shear areas – to the fundamental translational period of each building are developed. The structural periods could be determined from in-situ dynamic tests, full frame models or an appropriate period-height equation, the latter of which is provided here by calibrating from in-situ vibration tests of regional buildings constructed in compliance with British Standards. This simplified approach provides a fast track to seismic performance for both existing and new buildings, which could easily be comprehended by engineers without prior knowledge of seismic design.

Keywords: seismic, response spectrum analysis, low-to-moderate seismicity, Timoshenko beam

* Correspondence to Dr. R.K.L. Su, Department of Civil Engineering, The University of Hong Kong, Pokfulam Road, Hong Kong, PRC. E-mail: klsu@hku.hk

1. Introduction

Despite lying within a low-to-moderate seismicity region, it is not mandatory for buildings in Hong Kong (HK) to conform to any seismic design; as such, their vulnerability to seismic hazards is unpredicted. To rectify this deficiency, the implementation of a new seismic code for buildings is necessary. However, this requires a re-examination of the seismic resistance of existing buildings accompanied by retrofitting measures. Enormous workloads and unforeseeable consequences hinder stakeholders in their consenting to seismic code development. This densely-populated city, with its abundant skyscrapers of complex structural forms, is currently confronted by such dilemma. Simplified techniques for assessing the seismic performance of an immense volume of building stock are required.

Besides detailed nonlinear seismic analyses [1,2], simplified seismic assessment methods have aroused interest within the research field. Chopra has thoroughly summarized the contemporary simplified approaches (Chapter 22 in [3]). Amongst these, the coefficient-based method (CBM) is the most promising technique without resorting to a full frame model (e.g. Chapter 22.3.2 in [3], [4-10]). The semi-empirical-and-analytical drift factors are derived to account for the conversions from response spectral displacement (RSD) to roof drift ratio (RDR) and maximum interstory drift ratio (IDR). It allows the simplified assessment of buildings with various structural forms and even limited nonlinearity.

As one of the pioneers in CBM, Miranda [5, 6] has adopted a continuum approach to simplify the whole wall-frame building into a shear beam coupled with a flexural beam. Thus, drift factors could be analytically determined to correlate the RSD to RDR and IDR for a building. These studies delimit to buildings deforming only in the fundamental mode. Extending the model to account for a higher mode effect by modal superposition, Miranda and Akkar [7] assess the variations in IDR against the structural period under various damping ratios, lateral stiffness ratios, and higher modes. The equal displacement assumption for the shear and flexural beams along the building height renders their model different to the Timoshenko beam (TB) which couples the shear and flexural deformations in series. Besides, the conversions from RSD to RDR and IDR are actually spectrum-dependent, of which contributions from higher vibration modes may vary. Nonetheless, their studies suggest the potential caliber of a TB in the dynamic modeling of a real building and its compatibility with the CBM.

The use of a simple TB in modeling dynamic behavior of a real building was not prevalent until a verification study by Boutin et al. [11]. Two regular low-rise reinforced concrete (RC) buildings ranging from 22 m to 43 m high were investigated. From their tests, provided first and second frequencies were calibrated from an ambient vibration test (AVT), the uniform TB model was capable of simulating the third to fourth modal frequencies and first to third modal shapes compared to the experimental results. The detailed AVT results were included in a complementary paper by Hans et al. [12]. Followed by subsequent studies [13], they managed to repeat the tests on three 15 to 28 story prismatic RC buildings in France, which exhibited a coupled shear and flexural mode, indicating the essence of using a TB model.

Despite little influence on modal frequencies and shapes by soil-structure interaction (SSI) for buildings with shallow foundations reported in Boutin et al. [11], Cheng and Heaton [14] continue the research by introducing a soil spring at the base of a prismatic TB model to account for the flexibility of soil. They successfully reproduced first and second modal shapes of a nine-story RC frame building with a core wall situated on a stiff soil (with shear wave velocity SWV = 300 m/s) by matching the first and second frequencies. A similar assessment was also conducted on a prismatic 12 story RC shear wall building with one level basement by Kohler et al. [15], in which the predicted mode shape from the TB model was used to estimate the spatial-temporal response under an earthquake that matched well with seismic behavior of the 12-story concrete-shear wall building near downtown Los Angeles that has been instrumented with six community seismic network accelerometers.

The above findings prove the versatility of using a prismatic TB model in estimating the dynamic behaviors of a whole building. Yet, deficiency remains in the adaptability of this simple model to buildings with irregular lateral stiffness along the height, particularly for the high-rise building above a transfer frame, which is prevalent in HK. In addition, extraordinary second spectrum (a distinct set of natural frequencies with abnormal vibration modes) arises in the Timoshenko beam theory (TBT) once a critical frequency has been reached (f_c), and there has long been a controversial dispute among researchers as to whether it really exists (e.g. [16-20]). Boutin et al. [11] do not mention any potential influence and solution to addressing the second spectrum effect whereas Cheng and Heaton [14] delimit their study for buildings with eigen-frequencies below the critical frequency (f_c). This unfavorably renders low-rise squat buildings, vibrating in high frequency, out of the applicable scope.

The paper herein addresses all aforementioned issues by (a) the adoption of a two-segment TB model to simulate the building with irregularity along the elevation; (b) the extension of TBT in low-rise building modeling by investigating its numerical limitation; (c) in the case of compiled dynamic tests of regional buildings, their dynamic behaviors can be identified; (d) response spectrum analysis considering the first four modes are conducted on the calibrated TB models; thus, the simplified seismic assessment of buildings of various structural forms and building heights are allowed; and (e) simple design charts – in terms of the crucial seismic performance parameters namely RDR, IDR and shear area ratios – are provided in the relation with the fundamental structural period. Hence, preliminary seismic assessments can be conducted with ease once the structural period has been determined.

2. Use of Timoshenko beam models in simulating real buildings

2.1 Timoshenko beam theory

The cantilevered two-segment TB model employed in this study is briefly discussed herein. It has been developed from a prismatic TB model (e.g. [14, 18, 21]). Detailed derivations for the two-segment fixed-free TB model (boundary condition is fixed at one end and free at the other) adopted in this paper are provided in Appendix A, whilst its verifications are discussed in Section 3.

Based on the Hamilton's principle, the lateral deflection $\bar{W}$ and rotation $\bar{\Phi}$ of a TB conform to a fourth order spatial differential equation for each natural vibration mode. When its frequency $f <$ critical frequency $f_c = \frac{1}{2\pi}\sqrt{\frac{kGA}{\rho I}}$, the pure beam behavior (or the second spectrum) is not pronounced and the solution for $\bar{W}$ and $\bar{\Phi}$ is in hyperbolic-trigonometric form, as Eqs. (A29) and (A30); it becomes a trigonometric characteristic equation when $f > f_c$, as Eqs. (A34) and (A35). G and I are the equivalent shear modulus and moment of inertia of the TB model with plane area A equal to that of the building, factor $k = 2/3$ accounts for the uneven stress distribution across a rectangular section and ρ is the equivalent density of the buildings (≈ total mass/ total volume for a uniform building). As proved in the subsequent section, the relation between the frequency ratios of the higher modes to the first mode and the shear-to-flexural stiffness ratios (r_{sf}) is uniquely defined [11,14] for a uniform TB:

$$r_{sf} = \frac{\frac{kGA}{H_b}}{\frac{EI}{H_b^3}} = \frac{GH_b^2}{E}\frac{kA}{I} \quad (1a)$$

$$r_{sf} = \frac{GH_b^2}{E}\frac{8}{D^2} \quad (1b)$$

in which D is the span of the plane area along the vibrating direction, E is the equivalent Young's modulus and H_b is the total height of the building. For $r_{sf} \rightarrow +\infty$, the model degenerates into an Euler-Bernoulli beam with mainly flexural action and the frequency ratios for the second to fourth modes are close to 6.3, 17.4 and 34.0 respectively; whereas $r_{sf} \rightarrow 0$ refers to a pure shear beam and the corresponding frequency ratios diminish to 3, 5 and 7. Thus, provided the frequency ratio is obtained from AVTs or modeling, the r_{sf} factor for the TB model can easily be calibrated by matching the eigen-frequencies f_1 and f_2, where the subscript denotes the mode number. Despite the r_{sf}, the frequency ratio could vary with soil-structure interaction (SSI). The effects of SSI and slenderness ratios on frequency ratios are highlighted in Cheng and Heaton [14]. The effects of SSI on the frequency ratio (error $\leq$ 13%) and fundamental period (error $\leq$ 2.5%) become minimal for stiff soil foundation (shear wave velocity, SWV = 300 m/s) compared to the fixed ground condition. In light of the high SWV for soil in HK (usually $\geq$ 200 to 300 m/s), a mild influence is expected on the dynamic behavior of buildings. Despite the soil spring formulation following Cheng and Heaton [14] being incorporated in Appendix A, the effect of soil spring has been ignored in the following study for simplicity.

2.2 Dynamic behaviors of real buildings

A database comprised of mainly in-situ dynamic tests of buildings is compiled through literature review [11, 12, 14, 22-48] and previous site tests by the authors. All of these dynamic results were measured using accelerometers in ambient vibration tests, forced vibration tests or seismometers under real earthquakes. The two vital parameters – the first translational period and frequency ratios of higher modes – are investigated here. Reasonable ranges of these parameters would then be identified for subsequent TB model simulation to assess the seismic performance of buildings.

The sampled data encompasses a total of 75 buildings ranging from 15 m to 490 m high with the distribution shown in Fig. (3). They are mainly RC buildings with a rectangular, Y-, T- or L-shaped or cruciform layout plan, except for nine which are

composite or steel buildings. Their structural forms vary from simple shear wall, moment frame or in-filled frame buildings to high-rise coupled shear walls with core walls, tube-in-tube or outrigger belt truss, some of which are even situated above RC transfer plates or frames, causing the significant variation in lateral stiffness along the elevation. Table (1) summarizes the variations in the sampled buildings comprising the dimensions, the slenderness ratios and the r_{sf} factors calibrated from the measured second frequency ratio ($f_{r,2}$ = 2nd / 1st modal frequency along the same direction). Amongst the sampled buildings, 41 are regional moderate-to-high rise ($H_b \geq 40$ m) buildings in HK with a mean number of stories > 30 and a mean height > 100 m. Within this data pool, 21 buildings with known $f_{r,2}$ exhibit a r_{sf} ranging from 0.4 (shear-mode dominance) to 40 (flexural-mode dominance) with a median of about 10, considering both orthogonal directions. There is a paucity of dynamic test results from regional low-rise buildings, with only six samples having five to nine stories ($H_b < 40$ m), only one of which has a $f_{r,2}$ identified which exhibits a shear mode (r_{sf} = 0.2). Measurement of their higher modes is difficult due to the low participating mass ratios for higher modes as well as the sensitivity requirement of the equipment to precisely capture very high frequency responses. Yet, the limited result coincides with the expected shear mode behavior for the low-rise buildings. The above assessment of the dynamic test data outlines the significant ranges of dynamic properties suitable for the TB modeling and this will be discussed later in detail.

In accordance with Su et al. [25], the translational fundamental period of buildings varies with the construction materials, the structural form, usage (affecting gravity loads) and designed lateral load demands in addition to the non-structural components (e.g. partition walls, façade). Fig (4) depicts the measured fundamental period along either orthogonal direction against the building height. If the non-regional buildings are ruled out, a simple period-height equation can be deduced:

$$T_{\text{wall,i}} = 0.015H_b \qquad \text{for RC wall buildings} \qquad (2)$$

in which the subscript *i* refers to the intact period obtained from a small amplitude vibration. The relatively short period (compared to foreign buildings) is well justified by the denser partition walls of buildings in the densely-populated city of HK. Despite a larger load density of 5.5 kN/m^3 [25] in HK compared with 3.9 kN/m^3, for heavy and stiff shear wall buildings in the U.S[14], the period is shorter and it is attributed to the dense partition walls for small compartments. From Fig (4b), the lower- and upper-bound period-height equations can also be reasonably assumed by replacing the

coefficient 0.015 by 0.01 and 0.02, respectively. The above findings agree well with previous studies: Su et al. [25], based on eight RC frame, shear wall or mixed structural forms (50 m < H_b < 400 m), suggest $T_{wall,i}$ = 0.013H_b for regional buildings in HK; Campbell et al. [49] and Kwok et al. [47] suggest T = 0.015H_b from Tamura et al. [50], suiting well the RC buildings based on dynamic tests in HK; and Lagomarsino [51] recommends $T_{wall,i}$ = 0.0182H_b based on 52 RC tall buildings with heights of up to 200 m in Italy.

For low-rise RC frame building with in-fills, one may adopt Eq. (2) or the period-height equation of Eq. (3) in accordance with FEMA 450 [52]. For pure RC frame buildings, since there is a paucity of dynamic test results, it is recommended to follow EC8 [53] here:

$$T_{infilledframe,i} = 0.0488H_b^{(3/4)} \quad \text{for RC frame buildings with infill walls (FEMA 450)} \tag{3}$$

$$T_{frame,i} = 0.075H_b^{(3/4)} \quad \text{for RC frame buildings with } H_b \leq 40 \text{ (EC8)} \tag{4}$$

Fig. (4c) compares the estimated periods from Eqs. (2) to (4) for the low-rise buildings, whilst the measured fundamental translational periods from regional buildings are superimposed for verification. The dynamic tests for low-rise regional buildings are comprised of mainly the shear wall or in-filled frame buildings. Eq. (2) generally gives a closer match whereas Eq. (3), being close to 0.02H_b, forms almost an upper-bound estimate to the dynamic test results. Likewise, half of Eq. (3) or 0.01H_b could be set as the low-bound period for the low-rise in-filled frame buildings. The overstating by Eq. (3) is not unexpected as the trends of having higher periods in non-regional buildings are spotted earlier in Fig. (4b).

The above equations are based on tests from buildings under a modest vibration, and the cracking in structural elements under maximum considered earthquake (MCE) level is not accounted for. Despite this, different cracked stiffnesses are recommended in seismic codes (EC 8 [53], ACI318-11 [54], ASCE41-06 [55], NZS 1170.5:2004 [56], CSA A23.3-04 [57]), all of which require a suitably reduced stiffness to be considered in a seismic analysis. In agreement with both EC8 (cl.4.3.1(7)) and ACI318-11 (cl.8.8.2), a stiffness reduction factor of 0.5 applying to all elastic sectional properties is presumed herein, whereby:

$$\beta_i = 1/\sqrt{0.5} = 1.414 \quad (5)$$

in which β_i denotes the period lengthening effect when the RC elements crack under the MCE event. The above value is consistent with findings by different researchers determined from RC wall panel cyclic tests [58], full frame numerical modeling (β_i = 1.4 from Su et al. [59,60]) or shake table tests for various building types when concrete cracks notably: e.g. high-rise shear wall buildings above a transfer frame (β_i = 1.24 from Huang et al. [61]; $\beta_i \geq 1.3$ from Ye et al. [62]; first mode averaged β_i along X and Y direction = 1.2 to 1.7 after major to super-major earthquake by Li et al [63]) and in-filled RC frame buildings (e.g. β_i = 1.3 to 1.5 from four to seven story model tests by Liang and Chen [64]; β_i = 1.1 to 1.8 surveyed from four low-rise infilled RC frame shake table tests by Su et al. [10]).

From the database of sampled buildings, the measured second frequency ratios are calibrated against the 30 story TB model to obtain the corresponding r_{sf} factor. Although the frequency ratio for a constant r_{sf} varies with the height of TB, the changes are modest particularly for the lower modes. Thus they are neglected here for brevity. For $100 \leq r_{sf} \leq 0.001$, a closely matched trend line correlating the second frequency ratio ($f_{r,2}$) to r_{sf} from a regression analysis of results by the 30 story TB model is as follows (for $f_{r,2} \geq 2.8$):

$$r_{sf} = f_{r,2}^{\,4}(8.5192) + f_{r,2}^{\,3}(-126.68) + f_{r,2}^{\,2}(705.1) + f_{r,2}(-1724.2) + 1557.2 \quad (6)$$

Provided r_{sf} is estimated from measured $f_{r,2}$ using Eq. (6), the results of measured frequency ratios against r_{sf} of several buildings are depicted in Fig (5a). Fig (5a) clearly shows that the relationships between third (or fourth frequency ratio) and r_{sf} are highly closed to analytical result curve by linking third frequency ratio (or fourth frequency ratio) and r_{sf} derived from Eq. (6) together. Excellent agreement between the measured results and predicted results by TBT for higher frequency ratios of third and fourth modes shows the versatility of a prismatic TB model to simulate a whole building, if r_{sf} is reasonably assumed. The close proximity between the results along the shorter span and longer span indicates the compatibility of the TBT to simulate dynamic behaviors along both orthogonal directions. From the results shown in Table 1 and Fig. (5a), r_{sf} = 40 roughly indicates the maximum permissible bending behavior of the sampled buildings, whereas r_{sf} = 0.1 denotes the lowest r_{sf} for the pure shear behavior. By adopting this upper- and lower-bound r_{sf} for subsequent TB analysis, the actual building behavior likely lies in between. To avoid being over-conservative, the median value of r_{sf} = 10 is adopted for the following TB analysis of medium-to-high-rise shear wall buildings. It implies that $f_{r,2} \approx$ 3.55 to 3.75 are assumed for 14 to 40

story buildings, which is in close agreement with the findings by Su et al. [25] and Lagomarsino [51], which suggest the second frequency ratio = 3.57 and 3.76 respectively. Fig. 5(b) compares the frequency ratios for prismatic buildings with 16 and 30 stories predicted by TBT. It is noted that the TBT yields higher frequency ratios for the 30 story TB model for the higher mode and/or higher r_{sf}. Yet, such discrepancy almost vanishes for the second mode under limited r_{sf} (< 10). Hence, the assumption of using Eq. (6), derived from the 30 story TB model for estimating the r_{sf} from measured $f_{r,2}$, should remain acceptable.

3. Verification of Timoshenko beam model

3.1 Second spectrum of TBT

The issue of second spectrum for TBT was first discovered by Traill-Nash and Collar [65]. Since then, enormous efforts have been devoted to addressing the validity of second spectrum in Timoshenko beams under different boundary conditions (BCs) (e.g. [16-20]). Abbas and Thomas [16] investigate the two spectra of TBT by the constituents of three types of fundamental beams: the Euler-Bernoulli beam (large r_{sf}), simple shear beam (small r_{sf}) and pure shear beam (r_{sf} approaching to zero). The first spectrum of TBT generally follows asymptotically the Euler-Bernoulli beam properties and simple shear beam properties without inhabitation by the pure shear beam, as shown in Fig. 2(b). The second spectrum is generally classified as a set of eigen-frequencies exhibiting different characteristics to the first spectrum by TBT occurring when the eigen-frequency exceeds a threshold denoted by a critical frequency f_c. There is no doubt that the second spectrum exists for hinged-hinged BC (e.g. [16,17]). Yet, there are continuous debates on its existence in other BCs (e.g. [20]).

Since the second spectrum exhibits no distinctive characteristic in fixed-free BC [16], the difficulty in distinguishing the second spectrum was reported (e.g. [66]) and even its existence in fixed-free BC was disproved [16]. Conversely, the dominance of a pure shear beam effect when $f \geq f_c$ should not be disregarded for fixed-free BC. The first four modes of TBT have a great chance of exceeding f_c, particularly for a low slenderness beam with a large r_{sf}. This controversy could explain why Cheng and Heaton [14] delimit their study for $f \leq f_c$. For brevity, this problem could be bypassed in the current study with the results revealed from the dynamic tests of real buildings. Since low-rise buildings are mostly shear type buildings (small r_{sf}), they can be accurately modeled by TBT with a low r_{sf} factor, which is dominated by a simple shear beam behavior. In addition, the accumulated participating mass ratio for higher

modes in low-rise buildings is relatively modest (≤ 10 to 15%), limiting any errors introduced. Specific caution only has to be placed on medium-rise (e.g. ten story) buildings with significant bending behavior ($r_{sf} \geq 1$). Due to a paucity of dynamic tests on real buildings showing such behaviors, this type of building is not covered in this paper.

3.2 Verifications of the two-segment TB model

The free vibration of the fixed-free circular steel tube discussed in the computational example in Han et al. [18] is adopted here as a benchmark for verifying the two-segment TB model. Assuming each span is equal to half of the total length, an error of less than 0.1% in the estimated frequency, as shown in Table (2), and the good agreement between the modal shapes for the first four modes validates the two-segment TB model, as shown in Fig. (6). It is able to recover the results of a fixed-free prismatic TB model.

For the non-uniform two-segment TB model, its predictions are compared with the full frame model of a 134 m tall residential block in HK [59, 60]. It consists of a 36 story shear wall building situated on a six story transfer frame. The model was first established in the commercial package ETABS to allow for detailed seismic assessments. Response spectrum analysis is performed on both models along the shorter span using the site-specific soil spectrum in the paper [60].

To construct the TB model, the bottom frame and upper wall structures are constituted by the lower and upper TBs, respectively. The shear and flexural stiffness of the TB model is then calibrated to exhibit similar first and second modal frequencies. Unlike the uniform TB model, the second frequency ratio is no longer uniquely correlated with the r_{sf}. It is also influenced by the relative stiffness between the bottom frame and the upper wall structures. To simplify the calibration, the flexural bending stiffness for the bottom frame is set to be rigid, of which its deflection shape is dominated by shear coinciding with the expected behavior. The simplified TB model possesses constant plan dimensions = 14.8 m (depth) · 30 m (breadth) along the height, resulting in an equivalent plan area of 444 m^2 of the real model. By taking a pseudo r_{sf} = 15 (i.e. r_{sf} = 15 from Eq. (1b) by putting H_b = 134 m and D = 14.8 m) and assuming the shear stiffness ratio of the bottom frame to upper wall (G_b) is about 1.7 times; Table (3) summarizes the periods, participating mass ratios, modal RSA for the first four modes and the base shear, most of which show reasonable agreement.

Fig. (7a) depicts the modal shapes of the first four modes. Despite limited discrepancy along mid-story in the third and fourth modal shapes, the others match consistently. Fig. (7b) to (7d) respectively show the predicted story shear, displacement and IDR with the detailed results from ETABS. A displacement amplification factor (λ_{Rd}) due to torsion = 1.2, derived from the ETABS model, is assumed in the TB results. The three parameters are excellently simulated along the building height. Besides, the errors in the IDR, RDR and base shear are limited to 7.3%, 0.4% and -1.3% respectively, proving the versatility of the TB model to simulate buildings with non-uniform lateral stiffness and geometry along height.

4. Results and discussions

4.1 RSA demand and required shear area ratios

Fig. (8) shows the idealized uniform hazard spectra (UHS) adopted in this study. They are derived from a probabilistic seismic hazard assessment with a return period (RP) of 2475 years. Obviously, seismic induced loading by soil site dominates the design with a demand two to three times larger than that of the rock site. For the soil spectrum, which would be focused on in the following study, it is determined from the worst available soil class, from shallow to deep soil sites in HK. The corresponding SWV ≈ 200 to 300 m/s is equivalent to the type C soil class from Table 3.1 in EC8. The peak RSA, RSV and RSD of the 5% damped soil spectrum are 1.5 g, 870 mm/s and 250 mm respectively.

Response spectrum analysis is conducted on the TB model by summing the responses of the first four translational vibration modes using the square-root-of-the-sum-of-squared (SRSS) approach. The uniform TB model is first investigated. Building models are assumed to possess uniform lateral stiffness along a story with a constant height of 3 m and mass density of 5.5 kN/m^3 is adopted [25]. The accumulated participating mass ratio is ensured to reach the 90% minimum limit stipulated in seismic standards (e.g. cl.4.3.3.3.1(3) in EC8). The seismic demands computed from the uniform TB model on various building types are discussed below. Fig (9a) shows the RSA against first structural period for medium-to-high-rise shear wall buildings (assuming r_{sf} = 10) under a single direction earthquake. Presuming the structural period is equal to $T_{wall} = T_{wall,i} \cdot \beta_i$, the circle marks the predicted RSA for buildings of various heights: RSA for a 14 story building = 0.60 g, for a 20 story building = 0.48 g, for a 30 story building = 0.29 g and for a 40 story building = 0.21 g. Fig. (9b) simplifies the cumbersome need to calculate the structural period by normalizing the x-axis by the predicted period. Hence, the predicted demand is equal to the

interception of the demand curve and the vertical line (normalized period T/T_{wall} = 1), whereas the lower-bound and upper-bound periods are shown simultaneously with corresponding normalized periods = 0.66 and 1.33. For buildings of intermediate height, the seismic demands can be interpolated from the graph. More conservative RSA demands can be determined using lower-bound period ($0.01H_b \cdot \beta_i$) and the upper-bound r_{sf} = 40 determined from sampled AVTs (Table 1). A higher r_{sf} leads to larger frequency ratios and participating mass ratios for the higher modes. For r_{sf} = 40, it corresponds to an increase of 0% to 20% in RSA for 20 to 40 story buildings if T/T_{wall} = 0.66 and an increase of 20% to 40% for 20 to 40 story buildings if $1 \leq T/T_{wall} \leq 1.33$.

The seismic induced base shear can also be converted into the required minimum shear area. In accordance with capacity-based design, the mean strength of the material without reductions by material and load factors of safety is adopted. An overstrength factor is applied to protect the force-controlled members (e.g. shear resistance of walls and columns) to avoid unfavorable failure mechanism. For any walls or columns, shear stress is limited to $\Phi_{shear} \cdot 0.8\sqrt{(f_{cu,m})} \leq \Phi_{shear} \cdot 7$ MPa [60, 67] to avoid crushing of concrete, in which the incorporated factor of safety for shear Φ_{shear} = 1.25 is removed and mean cube strength of concrete ($f_{cu,m}$) = 1.4· characteristic cube strength ($f_{cu,k}$) is assumed, being consistent with the upper and lower-bound values = 1.3 and 1.7 for concrete in Priestley et al. [68]. To estimate the minimum required wall and column areas to sustain the MCE event, the averaged story shear stress should be restricted to $\Phi_{shear} \cdot 0.8\sqrt{(f_{cu,m})}/1.25 \approx \Phi_{shear} \cdot 0.6\sqrt{(f_{cu,m})}$, where the reduction factor = 1.25 limits the allowed degree of redistribution of shear load (cl.21.9.4.4 in ACI318-11). Thus the minimum required shear area in each direction is calculated by:

$$\frac{BaseShear_x}{0.8A_x} \cdot \lambda_T \lambda_R \Omega \leq \Phi_{shear} 0.6\sqrt{f_{cu,m}} \qquad \leq \Phi_{shear} \frac{7}{1.25} \text{ MPa} \qquad (7)$$

in which A_x denotes the total shear area = sum of wall and column areas at the ground level which contributes to the shear resistance (assumed in the x-direction here), and a reduction factor of 0.8 (cl.11.9.4 in ACI318-11) is assumed to account for the effective depth of walls; Ω = 1.5 denotes the load factor (overstrength factor) for the force-controlled member. For buildings on a sloping site with a slope angle ≥ 15°, a nominal topographic factor $\lambda_T \geq 1.2$ (Annex A in EC8 part 5 [69]) should be multiplied to the wall ratio. A nominal irregularity factor λ_R is also introduced: λ_R = 1 for regular buildings (e.g. conforming to both regularity requirements in plan and elevation from cl.4.2.3.2 to 4.2.3.3 in EC8), λ_R = 1.7 for irregular buildings or at least

λ_R = 2.5 for irregular buildings supported above transfer structures [59,70], in which gravity-induced shear stress = 2 to 3 MPa is assumed for the critical walls supported above the transfer [71]. The λ_R factor accounts for possible stress concentration effects on a single wall or column attributed to: (a) plan irregularity and (b) shear stress concentration on supported walls due to the transfer plate warping effect. From Eq. (7), the minimum required shear area ratio is calculated as = A_x/A, where A denotes the typical plan area of the building.

For brevity, $f_{cu,k}$ = 45 MPa, topographic factor λ_T = 1 and irregularity factor λ_R = 1 are assumed in deriving the following figures unless otherwise specified. Fig. (9c) depicts the shear area ratio for each orthogonal direction, ranging from 4% to 5% for 14 story to 40 story buildings. Likewise, the results can also be interpreted by normalizing the x-axis with the predicted period as shown in Fig. (9d). In this case, if the wall or column is not adequately reinforced to reach the maximum allowable shear stress, the shear strength on account of the practical shear steel provided should supersede the above shear limit and the above checking process should be repeated.

Almost a constant shear area ratio = 5% is attained between shear wall buildings of various heights in Fig. (9d). Since the structural period could vary due to the alignment of the in-plane direction of walls, the RSA and required shear area ratio may vary between the two orthogonal directions. For an identical layout in both directions, the total minimum shear area ratio would be equal to the sum = 10%. In cases where the vertical elements consist of only columns (e.g. the columns for a bottom transfer frame) which provide shear resistance in both orthogonal directions, the total column area ratio remains 5%. The above means allow engineers to determine the vulnerability of a specific building in terms of base shear resistance by solely measuring the wall and column area ratios at the critical floors (e.g. the ground floor and the floor just above transfer).

Since the λ_R provided above is only a ballpark figure, it could vary for buildings with unusual layouts. To assess a λ_R in detail, a multi-modal pushover (PO) analysis or RS analysis has to be conducted on the full frame model. Hence, the first yielding of the critical element can be identified which its yielding strength is reached. Hence, λ_R = the shear utilization rate of the critical member (= 1) divided by the averaged shear utilization rate of all walls and columns (≈ applied story shear stress/ total shear resistance of walls and columns). A similar procedure for assessing the RSA for the damage threshold is suggested by Boutin et al. [11] using the first mode PO on low-rise buildings. In general application, if the provided shear area ratio of a real building

is even less than the nominal demand for λ_R = 1, the building is liable to insufficient shear strength with a need for detailed seismic analysis.

For low-rise moment resisting frame buildings, the RSA and minimum shear area ratios against a normalized period with respect to T_{frame} (= $T_{frame,i}$·β_i) from Eq. (4) are plotted in Fig. (10), assuming a r_{sf} = 0.1. Compared to high-rise buildings, the RSA for a more rigid low-rise building is larger, ranging from 0.4 g to 1.3 g for buildings of various heights, but the minimum wall ratio required is less with lighter building masses. The minimum required shear area ratios range from 1.0% to 1.8% for the two to ten story pure frame buildings. In the presence of RC and/or masonry infills, the period could be stiffened (T/T_{frame} = 0.65 corresponds to Eq. (3)) resulting in a higher demand on the shear area ratios, ranging from 1.1% to 2.8% for two to ten story infilled frame buildings.

4.2 RDR, IDR and racking IDR demands

Deformations in terms of roof drift ratio (RDR = Δ_n/ H_b) and maximum interstory drift (IDR = max{(Δ_i - Δ_{i-1})/h_i}for i =1 to n) are usual design parameters for determining the performance state of a building (e.g. [68,72]) under various limit states, where Δ denotes the seismic induced lateral displacement, h is the story height and subscript i refers to the story number for a n-story building. For the collapse-prevention (CP) limit state, the RDR and IDR limits from CSA [57] = 1% and 1.5%, respectively, are adopted following Su et al. [60]. Such stringent limits are achievable only for the low-to-moderate seismicity region and could render the geometrical nonlinearity by P-delta effect in control [73, 74]. Comparatively, Vision 2000 report [75] suggests 1.5% IDR for the life safety (LS) limit state and 2.5% for the CP limit state; recent EC8 imposes a more stringent IDR limit of 0.5% to 1% on buildings with well attached to isolated non-structural components under 475-year-return-period earthquakes. Other code provisions generally adopt a much larger limit for the MCE event: PEER [73], LATBSDC [74] and AB83 [76] suggest a mean IDR limit of 3%.

The RDRs for high-rise wall buildings of various heights against period are depicted in Fig. (11a). Almost a constant RDR plateau is reached for periods beyond 2 sec, which conforms to the input spectrum with second corner period = 1.8 sec. Fig. (11b) shows RDR against the normalized period in accordance with T_{wall}. Compared to Fig. (11a), normalization with a height-dependent building period results in a unified gradient for RDR in Fig. (11b) and IDR and Fig. (11c). For the critical buildings with T/T_{wall} = 1.33, the maximum RDR and IDR are only 0.6% and 0.8%, respectively, indicating that limited nonlinearity is expected.

The displacement limits obtained from the graphs have to be amplified in the presence of unfavorable features: (a) for irregular buildings, an irregularity and torsional factor for displacement λ_{Rd} ranging from 1.2 to 1.7 is applied for high-rise shear wall buildings (detailed assessment of λ_{Rd} is similar to λ_R) and (b) a topographic factor $\lambda_T \geq 1.2$ is applied when it is on a sloping site with a slope angle $\geq 15°$. Thus, with these adverse conditions, the IDR for expected period ($T/T_{wall} = 1$) = 1.1% (= 0.55% · 1.7 · 1.2); whereas RDR = 0.9% (= 0.45% · 1.7 · 1.2). These are within the displacement limits, indicating that these medium-to-high-rise shear wall buildings are likely to sustain the MCE event without pronounced nonlinear behavior, i.e. satisfying the CP limit state for the MCE level. Particular cautions should be applied to flexible buildings ($T/T_{wall} = 1.33$): the IDR = 1.6% (= 0.8% · 1.7 · 1.2) and RDR = 1.2% (= 0.6 · 1.7 · 1.2), both of which slightly exceed the allowable limits.

Fig. (12a) and (12b) depict the variations of RDR and IDR, respectively, against the normalized period by T_{frame} for the low-rise buildings. The expected period for the low-rise in-filled frames or RC shear wall buildings is likely in between T/T_{frame} = 0.33 and 0.65 from Fig. (4c). Thus the critical IDR and RDR demands are limited to 1.0% and 0.65%, respectively, at $T/T_{frame} = 0.65$. Provided the shear area ratio in Fig. (10) is satisfied, these buildings could probably survive the MCE event. For low-rise pure frame buildings situated at the soil site, the critical IDR at the expected period ($T/T_{frame} = 1$) reaches 1.3% to 1.6% for buildings of ten to two stories tall. Notable nonlinear behavior could be developed especially for any RC walls and infilled frames that present. In addition, if unfavorable features like irregularity ($\lambda_{Rd} \approx 1.7$) and topographic factor ($\lambda_T = 1.2$) exist, most low-rise buildings are susceptible to damage by exceeding the drift limit. This implies that (a) the assumption for 5% inherent viscous elastic damping is too conservative, (b) the period-height equation understates the structural period without accounting for the global ductility attained in the building and (c) the geometrical nonlinearity by P-Delta could be significant and should be adequately accounted for.

And the definition of racking inter-story drift ratio (Racking IDR) is the difference between inter-story drift ratio and floor rotation angle. Comparatively, the racking IDR from the shear displacement is closely commensurate with the IDR for low-rise shear-type buildings, which is not duplicated here; whereas the racking IDR for medium-to-high-rise wall buildings is about half of the IDR as depicted in Fig. (11d). It declines with increasing r_{sf} for high-rise buildings.

4.3 Non-uniform TB model for buildings with transfer structures

To model the building supported on a transfer frame, the flexural stiffness of the bottom beam, resembling the transfer structure with high rotational rigidity, is assumed to be infinite. Fig. (13) compares the results with and without rigid flexural stiffness assumption, where the E_b denotes the flexural stiffness of the bottom beam (bottom frame) compared to the upper beam (upper walls) and the symbols +1F and +5F denote the number of stories for the bottom transfer frame with a constant story height of 5 m.

The model with E_b = 1 resembles the uniform TB model. In general, the changes in RDR are modest, whereas the shear area ratio reduces slightly for the five story transfer with rigid E_b due to a notable alteration of r_{sf}. A more noteworthy effect is the IDR being amplified by 13% (T/T_{wall} = 1.0) for transfers with rigid E_b, whereas the racking IDR is also increased by 44%. To explain such phenomenon, detailed IDR and story displacement for the five story transfer with E_b = 1 and rigid E_b are compared in Fig. (14) at expected period, T_{wall} = 2.43 sec (or T/T_{wall} = 1.0). Although the story displacements are similar for the models with E_b = 1 or infinite, the IDR of the latter model is reduced along the height of the transfer conforming to the expected shear displacement profile, whilst the upper shear wall exhibits a larger IDR. A larger racking IDR is also mobilized.

By providing a spacious area for recreational or commercial purposes, the lateral stiffness of the bottom frame is usually reduced. This effect is simulated by reducing the shear stiffness of the bottom frame to 20% of shear stiffness (G_b = 0.2) and 50% (G_b = 0.5) with results shown in Fig. (15), presuming a rigid E_b. An example of G_b = 5 indicating a stiffened bottom frame is also presented. The required shear area ratio or RSA is directly proportional to the increase in G_b, whilst a similar increasing trend in IDR is observed for G_b = 0.5 to 5. Stiffening of the bottom frame induces a more fierce vibration mode and IDR at the upper walls. An exception is observed in IDR for models with G_b = 0.2, in which the over-softening of the bottom frame stiffness results in a dominant shear-type first vibration mode contributing to over 80% participating mass. Its IDR and racking IDR are amplified significantly at the soft story of the transfer frame. The racking IDR is inversely-proportional to G_b. For models with $G_b \leq 0.5$, the IDR closely matches the racking IDR, indicating that the maximum deformation is dominated by the soft story at the bottom frame.

The high-rise residential building in HK typically possesses a shear area ratio ranging from 9% to 13% for the sampled public housing blocks, indicating that the expected shear area ratios from Fig. (9) and Fig. (15) are achievable provided they are not over-

stiff. Buildings having sufficient shear area ratios and limited IDR and RDR could be deemed to be satisfactory in seismic performance. Conversely, others susceptible to insufficient shear resistance could easily be identified for further detailed analysis. For instance, the 134 m tall building above a six story transfer frame, mentioned in Section 3, is analyzed here as an illustration. The building is composed of C40 ($f_{cu,k}$ = 40 MPa) RC walls and columns with shear area ratios of 6.9% above and 7.3% below the transfer, which shows a satisfactory performance in the detailed seismic analysis using ETABS by Su et al. [59,60]. The first translational periods of the building along shorter and longer spans are close to 5.0 sec and 4.8 sec respectively.

From Fig. (15), assuming the building could be approximately modeled as a 30+5F building with r_{sf} = 10, G_b = 5, T/T_{wall} = 2 and λ_{Rd} = 1.2 (determined in Section 3); the estimated IDR demand = 0.56% (= 0.9% · (130/250) · λ_{Rd}), RDR = 0.22% (= 0.35% · (130/250) · λ_{Rd}), where the ratio 130/250 accounts for the lower peak RSD (≈ 130 mm) in the site-specific spectrum employed [60]. For RSA, it is estimated as = 0.080 g (= 0.11 g · 130/250 · 1.4), where the 1.4 factor conservatively accounts for the RSA increase due to the higher r_{sf} involved for the building discussed in Section 4.1. They closely approximate the detailed RS analysis results from ETABS [60] showing an IDR = 0.58%, RDR = 0.22% and RSA = 0.071 g. For the predicted shear area ratios, it is = 1.6% (= 2.1% · (130/250) · 1.4 · √(45/40)) under a single direction earthquake. Thus, the total shear area ratio for resisting bi-directional earthquake = 1.6% · 2 = 3.2%. Provided the shear area ratios = 6.9% above and 7.3% below the transfer, the estimated shear utilization ratio (URV_{max} = shear demand/capacity) for the critical wall = 0.87 (= 3.2%/ 6.9% · λ_R · (0.6/0.8)) above the transfer and for the column = 0.41 (= 3.2%/7.3% · λ_R · (0.6/0.8) /2), in which λ_R = 2.5 and factor 0.6/0.8 denote the shear concentration and higher shear limit for an individual wall compared to the story shear discussed in Section 4.1; a reduction factor 1/2 is further applied to the transfer columns on account of the bi-directionally effective shear area. Compared to the detailed analysis, URV_{max} = 0.9 for the critical upper wall and 0.4 for the bottom frame column [60]. The close approximations of IDR, RDR, RSA and shear area demands exemplify the versatility of this simplified seismic assessment approach.

5. Concluding remarks

Attributed to the surging concern about the seismic risk of un-conforming buildings to seismic design for a well-developed city, a comprehensive seismic assessment tool has been developed and presented in this paper. A two-segment Timoshenko beam model with a fixed-free BC has been adopted to simulate the dynamic behavior of buildings with a variety of structural forms and building heights. Upon performing

response spectrum (RS) analysis on the TB model considering the first four vibration modes, the predicted seismic responses have been successfully verified against the full frame model of a high-rise shear wall building supported on a transfer frame. In compliance with the in-situ dynamic tests of local buildings, a typical period-height equation (T) and shear-to-flexural stiffness factor (r_{sf}) are determined for the high-rise shear wall buildings and low-rise frame or in-filled frame buildings. These outline the crucial inputs for allowing simplified seismic assessments using a TB model.

Design charts for correlating seismic demands – RSA, RDR, IDR, racking IDR and shear area demands – with fundamental translational structural periods have been proposed. In essence, they resemble the single-degree-of-freedom response spectra. However, utilizing a TB model extends the applicability to cover different structural forms and building heights. Satisfactory buildings are required to simultaneously conform to the minimum shear area ratios (or RSA), RDR and IDR limits determined. Under the low-to-moderate seismicity demands with a RP = 2475 years, it is probable that medium-to-high-rise buildings with or without a transfer will sustain the MCE event without inducing much nonlinear behavior. Conversely, a conjunction of unfavorable features – e.g. irregular buildings located on a sloping site – could render the low-rise pure frame buildings susceptible to severe damage by exceeding the drift limits under the design soil spectrum. Detailed analysis catering for the ductility and corresponding damping is required to further assess the vulnerability of these critical buildings.

Overall, the assessment method proposed here allows freedom for users to substitute the intact period by either (a) the accurate prediction from in-situ dynamic tests, (b) full frame models or (c) the approximation by period-height equations. Conservatively, the expected structural period could be chosen as a lower-bound or upper-bound estimate depending on the interest demand. The novelty of the proposed simplified design charts allows even an amateur to comprehend a preliminary seismic assessment for various types of buildings whilst sufficient accuracy is maintained. It is particularly useful for assessing an immense number of un-conforming building stocks liable to unknown seismic risks, providing an invaluable insight on critical buildings for further assessment or retrofitting needs.

Acknowledgement
The authors are grateful of the support provided by the Small Project Funding from The University of Hong Kong.

REFERENCES

[1] Brunesi, E., Nascimbene, R., Parisi, F.,& Augenti, N. (2015). Progressive collapse fragility of reinforced concrete framed structures through incremental dynamic analysis, *Engineering Structures*, 104, 65-79

[2] Minghini, F., Bertolesi, E., Del Grosso, A., Milani, G., Tralli, A., (2016). Modal pushover and response history analyses of a masonry chimney before and after shortening, *Engineering Structures*, 110, 307-324

[3] Chopra, A.K. (2007). Dynamics of Structures: Theory and Applications to Earthquake Engineering, 3rd edition.

[4] Federal Emergency Management Agency (*FEMA 356*). (2000). *Prestandard and Commentary for the Seismic Rehabilitation of Buildings*, *Report FEMA 356*, Washington D.C., USA.

[5] Miranda, E. (1999). Approximate seismic lateral deformation demands in multistory buildings. *Journal of Structural Engineering, ASCE*, 125(4), 417-425.

[6] Miranda, E., Reyes, C.J. (2002). Approximate Lateral Drift Demands in Multi-story Buildings with Non-uniform Stiffness. *Journal of Structural Engineering*, 128(7), 840–849.

[7] Miranda, E., Akkar, S.D. (2006). Generalized Inter-story Drift Spectrum. *Journal of Structural Engineering*, 132(6), 840–852.

[8] Zhu, Y., Su, R.K.L, & Zhou, F. (2007). Cursory seismic drift assessment for buildings in moderate seismicity regions. *Earthquake Engineering and Engineering Vibration*, 6(1), 85-97.

[9] Tsang, H.H., Su, R.K.L., Lam, N.T.K., & Lo, S.H. (2009). Rapid Assessment of Seismic Demand In Existing Building Structures. *The Structural Design of Tall and Special Buildings*, 18, 427–439.

[10] Su, R.K.L., Tang, T.O., & Lee, C.L. (2013). Evaluation of local and global ductility relationships for seismic assessment of regular masonry-infilled reinforced concrete frames using a coefficient-based method. *Earthquakes and Structures*, 5(1), 1-22.

[11] Boutin, C., Hans, S., Ibraim, E., & Roussillon, P. (2005). In-situ experiments and seismic analysis of existing buildings. Part II: Seismic integrity threshold. *Earthquake Engineering and Structural Dynamics*, 34 (12), 1531-1546.

[12] Hans, S., Boutin, C., Ibraim, E., & Roussillon, P. (2005), In situ experiments and seismic analysis of existing buildings, Part I: Experimental investigations. *Earthquake Engineering and Structural Dynamics*, 34(12), 1513–1529.

[13] Michel, C., Hans, S., Gueguen, P., & Boutin, C. (September 2006). In-Situ

Experiment and Modeling of RC-Structure using Ambient Vibration and Timoshenko Beam. *First European Conference on Earthquake Engineering and Seismology, Geneva, Switzerland*, 3-8, 1246.

[14] Cheng, M.H., Heaton, T. (2013). Simulating building motions using the ratios of its natural frequencies and a Timoshenko beam model. *Earthquake Spectra*.

[15] Kohler, M.D., Heaton, T.H., & Cheng, M.H. (2013). The community seismic network and quake-catcher network: enabling structural health monitoring through instrumentation by community participants. *Proc. SPIE 8692, Sensors and Smart Structures Technologies for Civil, Mechanical, and Aerospace Systems*. 8692, 86923X1-8.

[16] Abbas, B.A.H, Thomas, J. (1997). The second frequency spectrum of Timoshenko beams. *Journal of Sound and Vibration*, 51(1), 123–137.

[17] Bhashyam, G.R., Prathap, G. (1981). The second frequency spectrum of Timoshenko beams. *Journal of Sound and Vibration*, 76(3), 407–420.

[18] Han, S.M., Benaroya, H., Wei, T. (1999). Dynamics of transversely vibrating beams using four engineering theories. *Journal of Sound and Vibration*, 225(5), 935–988.

[19] Stephen, N.G. (2006). The second spectrum of Timoshenko beam theory—further assessment. *Journal of Sound and Vibration*, 292, 372–389.

[20] Díaz-de-Anda, A., Flores, J., Gutiérrez, L., Méndez-Sánchez, R.A., Monsivais, G., & Morales, A. (2012). Experimental study of the Timoshenko beam theory predictions. *Journal of Sound and Vibration*, 331(26), 5732-5744.

[21] Wang, C.M., Zhang, Y.Y., & He, X.Q. (2007). Vibration of nonlocal Timoshenko beams. *Nanotechnology*, 18, 1-9.

[22] Li, Q.S., Xiao, Y.Q., Wong, C.K., & Jeary, A.P. (2003). Field measurements of wind effects on the tallest building in Hong Kong. *The Structural Design of Tall and Special Buildings*, 12(1), 67–82.

[23] Li, Q.S., Wong, C.K., Fang, J.Q., Jeary, A.P., & Chow, Y.W. (2000). Field measurements of wind and structural responses of a 70-story tall building under typhoon conditions. *The Structural Design of Tall Buildings*, 9(5), 325–342.

[24] Ko, J.M., Bao, Z.W. (editors). (1985). Ambient Vibration Measurements on Existing Tall Buildings in Hong Kong. Hong Kong Polytechnic & Qinghua Universities.

[25] Su, R.K.L., Chandler, A.M., Lee, P.K.K., To, A.P., & Li, J.H. (2003). Dynamic Testing and Modelling of Existing Buildings in Hong Kong, *Transactions of Hong Kong Institution of Engineers*, 10(2), 17-25.

[26] Wong, C.K. (2001). Identification of non-linear damping of tall buildings by

the random decrement. *Ph.D dissertation*. City University of Hong Kong.

[27] Brownjohn, J.M.W. (2003). Ambient vibration studies for system identification of tall buildings. Earthquake Engineering & Structural Dynamics, 32(1), 71–95.

[28] Li, Q.S., Yang, K., Zhang, N., Wong, C.K., & Jeary, A.P. (2002). Field measurements of amplitude-dependent damping in a 79-storey tall building and its effects on the structural dynamic responses. *The Structural Design of Tall Buildings*, 11(2), 129–153.

[29] Xu, Y.L., Zhan, S. (2001). Field measurements of Di Wang Tower during Typhoon York. *Journal of Wind Engineering and Industrial Aerodynamics*, 89(1), 73–93.

[30] Memari, A.M., Aghakouchak, A.A., Ghafory Ashtiany, M., & Tiv, M. (1999). Full-scale dynamic testing of a steel frame building during construction. *Engineering Structures*, 21(12), 1115–1127.

[31] Li, Q.S., Fang, J.Q., & Jeary, A.P. (2000). Free vibration analysis of cantilevered tall structures under various axial loads. *Engineering Structures*, 22(5), 525-534.

[32] Çelebi, M. (2003). Identification of Site Frequencies from Building Records. *Earthquake Spectra*, 19(1), 1-23.

[33] Tena‐Colunga, A., Valle, E.D., & Prez‐Moreno, D. (1996). Issues on the Seismic Retrofit of a Building near Resonant Response and Structural Pounding. *Earthquake Spectra*, 12(3), 567-597.

[34] Brownjohn, J.M.W., Pan, T.C., Cheong, H.K. (1998). Dynamic Response of Republic Plaza, Singapore. *The Structural Engineer*, 76(11), 221-226.

[35] Watakabe, M., Tohdo, M., Chiba, O., Izumi, N., Ebisawa, H., & Fujita, T. (2001). Response control performance of a hybrid mass damper applied to a tall building. *Earthquake Engineering & Structural Dynamics*, 30(11), 1655–1676.

[36] Saito, T., Shiba, K., & Tamura, K. (2001). Vibration control characteristics of a hybrid mass damper system installed in tall buildings. *Earthquake Engineering & Structural Dynamics*, 30(11), 1677–1696.

[37] Zaicenco, A., Alkaz, V. (2001). Seismic tests on a 16-storey cast-in-place r/c building, and stochastic simulation results. *The Structural Design of Tall Buildings*, 10(1), 69–77.

[38] Nagashima, I., Maseki, R., Asami, Y., Hirai, J., & Abiru, H. (2001). Performance of hybrid mass damper system applied to a 36-storey high-rise building. *Earthquake Engineering & Structural Dynamics*, 30(11), 1615–1637.

[39] Lee, L.H., Chang, K.K., & Chun, Y.S. (2000). Experimental formula for the

fundamental period of RC buildings with shear-wall dominant systems. *The Structural Design of Tall Buildings*, 9(4), 295–307.

[40] Bradford, S.C. (2006). Time-frequency analysis of systems with changing dynamic properties. *Ph.D dissertation*. California Institute of Technology. Pasadena, California.

[41] Kim, J.Y., Yu, E., Kim, D.Y., & Kim, S.D. (2009). Calibration of analytical models to assess wind-induced acceleration responses of tall buildings in serviceability level. *Engineering Structures*, 31(9), 2086–2096.

[42] Campbell, S., Kwok, K.C.S., & Hitchcock, P.A. (2005). Dynamic characteristics and wind-induced response of two high-rise residential buildings during typhoons. *Journal of Wind Engineering and Industrial Aerodynamics*, 93(6), 461–482.

[43] Kuang, C.L., Kwok, K.C.S., Hitchcock, P.A., & Ding, X.L. (2011). Wind-Induced Response Characteristics of a Tall Building from GPS and Accelerometer Measurements *Positioning*, 2(1), 13 pages.
DOI: 10.4236/pos.2011.21001.

[44] Li, Q.S., Wu, J.R., Liang, S.G., Xiao, Y.Q., & Wong, C.K. (2004). Full-scale measurements and numerical evaluation of wind-induced vibration of a 63-story reinforced concrete tall building. *Engineering Structures*, 26(12), 1779–1794.

[45] Feng, M.Q., Kim, J.M., & Xue, H. (1998). Identification of a dynamic system using ambient vibration measurements. *Journal of Applied Mechanics*, 65(4), 1010–21.

[46] Li, Q.S., Xiao, Y.Q., Fu, J.Y., & Li, Z.N. (2007). Full-scale measurements of wind effects on the Jin Mao building. *Journal of Wind Engineering and Industrial Aerodynamics*, 95(6), 445–466.

[47] Kwok, K., Tse, K., & Campbell, S. (2011). Field measurements of dynamic properties of high-rise buildings. *Advances in structural engineering*, 14(6), 1107-1128.

[48] He, Y.C., Li, Q.S. (2014). Dynamic responses of a 492-m-high tall building with active tuned mass damping system during a typhoon. *Structural Control and Health Monitoring*, 21(5), 705–720.

[49] Campbell, S., Kwok, K.C.S., Hitchcock, P.A., Tse K.T., & Leung H.Y. (2007). Field Measurements of Natural Periods of Vibration and Structural Damping of Wind-Excited Tall Residential Buildings. *Wind and Structures*, 10(5), 401-420.

[50] Tamura, Y., Suda, K., & Sasaki, A. (2000). Damping in buildings for wind resistant design. *Proc. Int'l Symp. on Wind and Structures* (Cheju), Techno-

Press, Korea, 115-130.

[51] Lagomarsino, S. (1993). Forecast models for damping and vibration periods of buildings. *Journal of Wind Engineering and Industrial Aerodynamics*, 48(2-3), 221-239.

[52] Building Seismic Safety Council, BSSC. (2004). *NEHRP Recommended Provisions for Seismic Regulations for New Buildings and Other Structures (FEMA 450)*, Washington, D.C.

[53] CEN. (2004). *Eurocode 8: Design of Structures for Earthquake Resistance, Part 1: General Rules, Seismic Actions and Rules for Buildings, ENV 1998-1:2004*, Comité Européen de Normalisation, Brussels, Belgium.

[54] ACI Committee 318. (2011), *Building Code Requirements for Structural Concrete (ACI 318-11) and Commentary*, American Concrete Institute, Farmington Hills, MI.

[55] ASCE. (2007). *Seismic Rehabilitation of Existing Buildings, ASCE/SEI 41-06*, American Society of Civil Engineers, Reston, Virginia,.

[56] SNZ. (2004). *Structural Design Actions Part 5: Earthquake Actions – New Zealand, NZS 1170.5:2004*, Standards New Zealand, Wellington, New Zealand.

[57] CSA Committee. (2004). *Design of Concrete Structures*, *CSA A23.3-04*, Canadian Standards Association, Mississauga, Canada.

[58] Tang, T.O., & Su, R.K.L. (2014). Shear and flexural stiffnesses of reinforced concrete shear walls subjected to cyclic loading. *Open Construction and Building Technology Journal*, 8, 104-121.

[59] Su, R.K.L., Keung, W.C., Tang, T.O., & Looi, D.T.W. (2004). Analysis and design of irregular tall buildings in Hong Kong by a strength-based design approach, The Proceedings of the *4th International Conference on Structural Engineering and Construction Management*, 13-15 December 2013, Kandy, Sri Lanka. Volume 1, 16-28.

[60] Su, R.K.L., Looi, D.T.W., Tang, T.O., & Law, C.W. (2014). Performance Based Seismic Design for Tall Buildings in Hong Kong. *Joint Structural Division Annual* Seminar, *Hong Kong*.

[61] Huang, X., Jin, J., Zhou, F., Yang, Z., & Luo, X. (2004). Seismic Behavior Analysis of a High-rise Building of Frame-Shear Wall Structure with High Transfer Floor, *Earthquake Engineering and Engineering Vibration*, 24(3), 73-81. (In Chinese)

[62] Ye, Y., Liang, X., Yin, Y., Li, Q., Zhou, Y., & Gao, X. (2003). Seismic Behavior and Design Suggestions on Frame Supported Shear Wall structures in high-rise Buildings. *Structure Engineers*, 4, 7-12. (in Chinese)

[63] Li, C., Lam, S., Zhang, M., & Wong, Y. (2006). Shaking Table Test of a 1:20

Scale High-Rise Building with a Transfer Plate System. *Jorunal of Structural Engineering*, 132(11), 1732–1744.

[64] Liang, S.H., Chen, Z.F. (2006). Research on the formula of vibration period about masonry structure supported by frame, *Jiangsu Jian Zhu*, 107(4), 18-20. (In Chinese)

[65] Traill-Nash, R.W., Collar, A.R. (1953). The effect of shear flexibility and rotary inertia on the bending vibrations of beams. *Quarterly Journal of Mechanics and Applied Mathematics*, 6, 186–222.

[66] Tobe, T., Sato, K. (1973). Lateral vibrations of cantilevers considering the effects of rotary inertia, shear flexibility and solid viscosity. *Bulletin of the Japanese Society of Mechanical Engineers*, 16, 696-703.

[67] BD. (2013). *Code of Practice for Structural Use of Concrete 2013*. Buildings Department (BD), the Government of the HKSAR, Hong Kong.

[68] Priestley, M., Calvi, G., & Kowalsky, M. (2007). Displacement-based seismic design of structures, IUSS Press, Pavia, Italy.

[69] CEN. (2004). *Eurocode 8: Design of Structures for Earthquake Resistance, Part 5: Foundations, retaining structures and geotechnical aspects, ENV 1998-5:2004*, Comité Européen de Normalisation, Brussels, Belgium.

[70] Su, R.K.L., Cheng, M.H. (2008). Earthquake Induced Shear Concentration in Shear Walls above Transfer Structures. *The Structural Design of Tall and Special Buildings*, 18(6), 657-671.

[71] Tang, T.O., Su, R.K.L. (2015). Gravity-induced Shear Force in Walls above Transfer Structures. *Structures and Buildings*, 168(1), 40-55

[72] CTBUH. (2008). Recommendations for the Seismic Design of High-rise Buildings, Council of Tall Buildings and Urban Habitat (CTBUH), Chicago, IL.

[73] Pacific Earthquake Engineering Research Center (2010). "Guidelines for Performance-Based Seismic Design of Tall Buildings," *PEER Report 2010/05*, prepared by the TBI Guidelines Working Group, Berkeley, California.

[74] LATBSDC. (2011).An Alternative Procedure for Seismic Analysis and Design of Tall Buildings Located in the Lo s Angeles Regions, Los Angeles Tall Buildings Structural Design Council, CA.

[75] SEAOC. (1995). *Vision 2000 Report–Performance-based Seismic Engineering of Buildings*, SEAOC Vision 2000 Committee, Structural Engineers Association of California (SEAOC).

[76] AB83. (2010). Requirements and Guidelines for the Seismic Design of New Tall Buildings using Non-Prescriptive Seismic-Design Procedures, 2010 San Francisco Building Code.

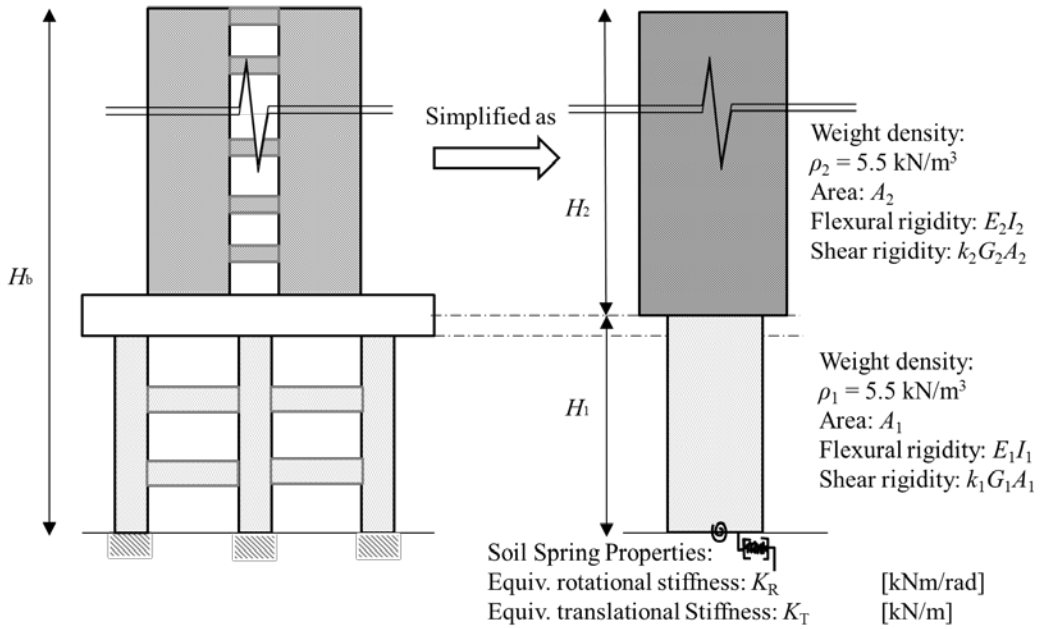

Fig. 1. Notations of properties for formulating the non-uniform Timoshenko beam.

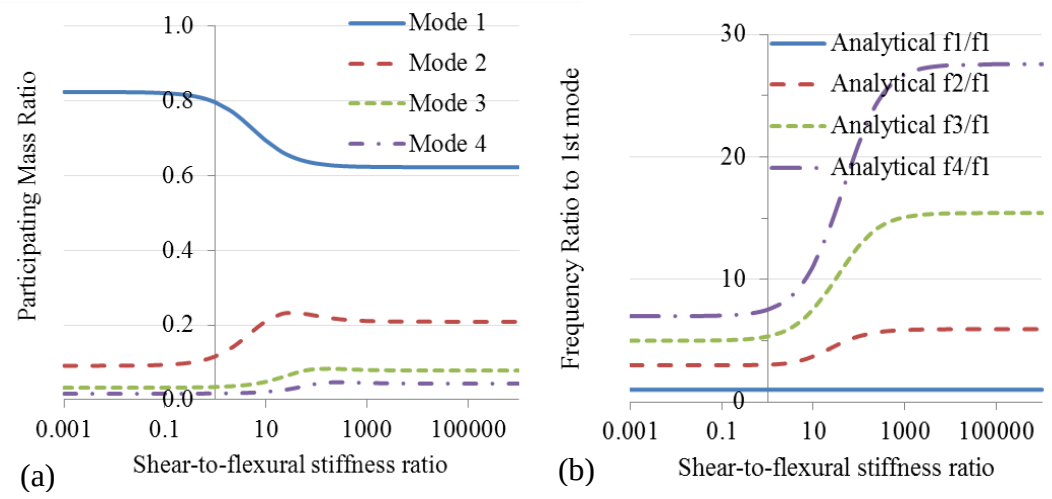

Fig. 2. Effect of shear-to-flexural stiffness ratios on (a) participating mass ratios and (b) frequency ratios (30F Uniform Building).

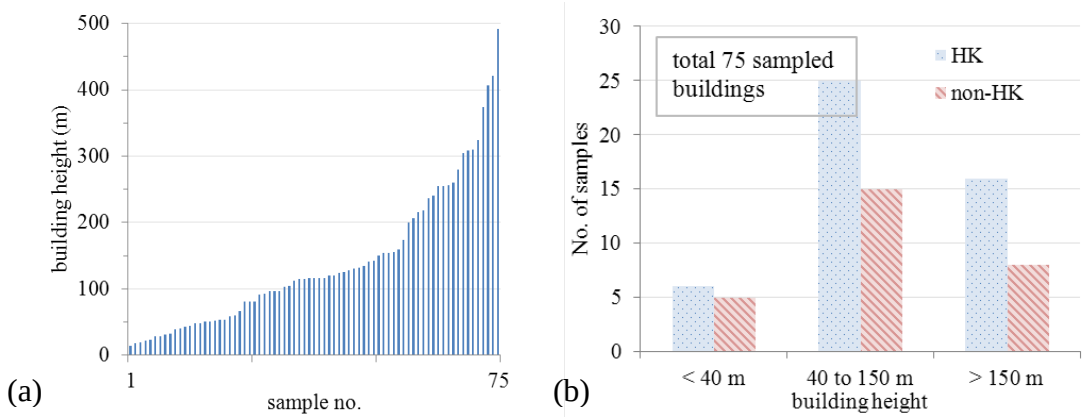

Fig. 3. Building height distribution of the sampled buildings.

		Sample No.	max	min	mean	median	CoV
Building total Height, H_b (m)		75	492	14.1	140.4	116.4	0.76
No. of story		59	88	6	33.9	34	0.62
Plan Dimensions (m)	- shorter span	42	58.0	8.8	30.4	30	0.47
	- longer span	42	110.0	15.9	43.2	45	0.44
slenderness ratio	- shorter span	41	13.7	1.3	4.2	3.0	0.71
	- longer span	41	12.4	0.6	3.0	2.3	0.80
shear-to-flexural stiffness ratios (all buildings)	- shorter span	34	39.8	0.2	13.4	13.4	0.61
	- longer span	32	41.9	0.4	9.0	8.0	0.85
shear-to-flexural stiffness ratios (only regional buildings and H_b > 40 m)	- shorter span	21	39.8	4.8	14.7	13.1	0.56
	- longer span	21	41.9	0.4	9.0	7.4	0.97

Table 1. Ranges of characteristics for the sampled buildings.

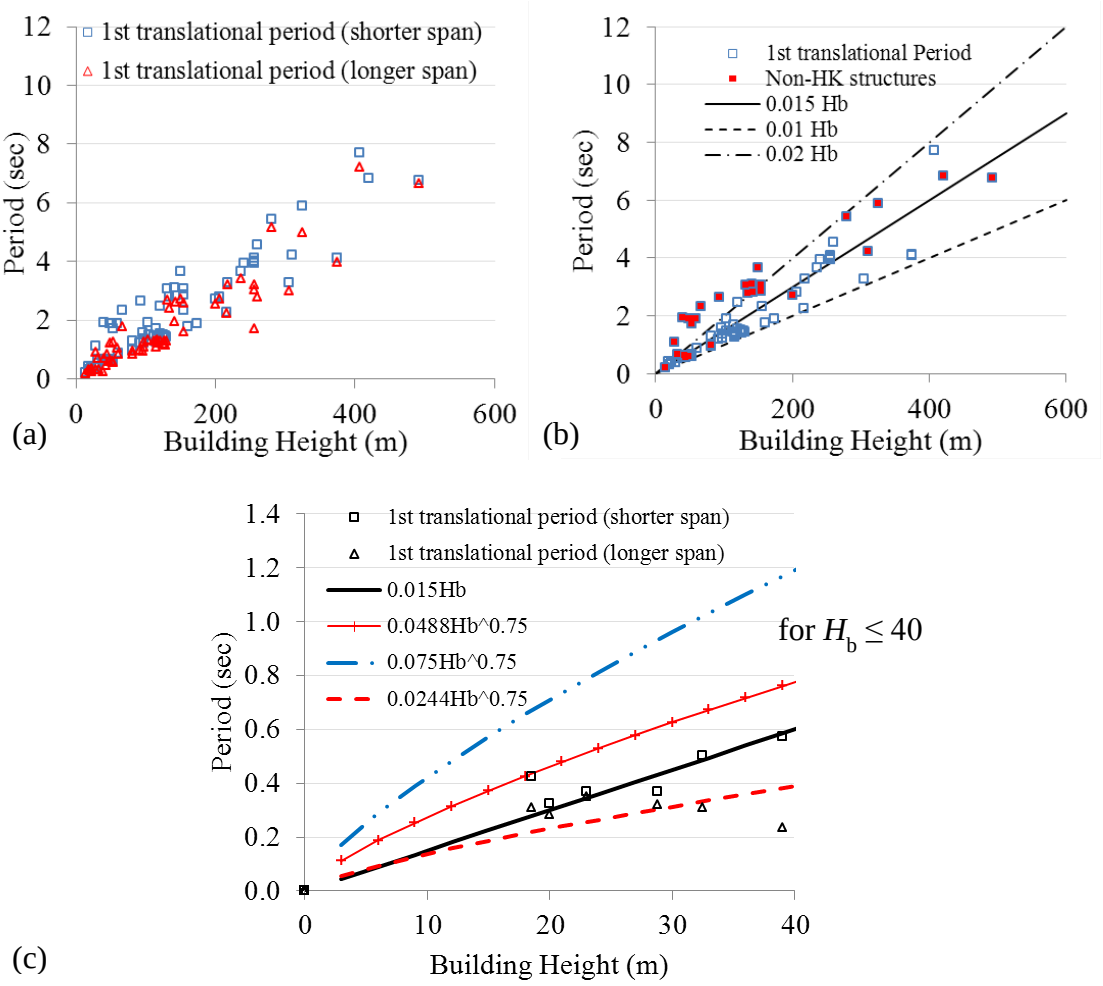

Fig. 4. Comparisons of first translational periods against the building height derived from in-situ dynamic tests: (a) in two orthogonal principal directions; (b) in the shorter span for regional and non-regional buildings; and (c) for low-rise regional buildings ($H_b \leq 40$).

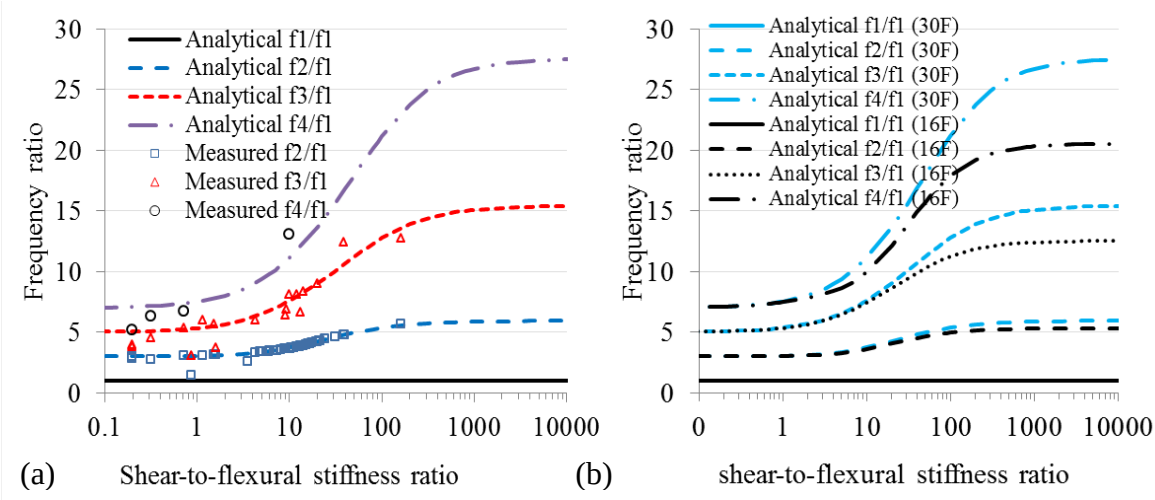

Fig. 5. Comparisons of frequency ratios against shear-to-flexural stiffness ratios (r_{sf}) for (a) experimental results (symbols) and analytical results from a uniform 30 story TB (lines); and (b) analytical results from uniform TBs of different story numbers.

	Estimation by the two-segment TB model	Computed Results from Han et al. [16]
mode	Frequency(Hz)	Frequency(Hz)
1	269.93	269.93
2	1077.3	1077.2
3	2270.9	2270.7
4	3249.6	3249.2
5	4003.3	4002.8
6	4649.7	4649.2
7	5378.7	5378.2
8	6049.1	6048.4
9	7156.0	7155.4
10	7385.6	7385.1
11	8465.3	8464.4
12	9366.9	9366.1
13	9797.4	Not Provided

Table 2. Comparison of computed frequencies for a clamped-free uniform steel tube in Han et al. [16] ($f > f_c$ for mode 5 onwards).

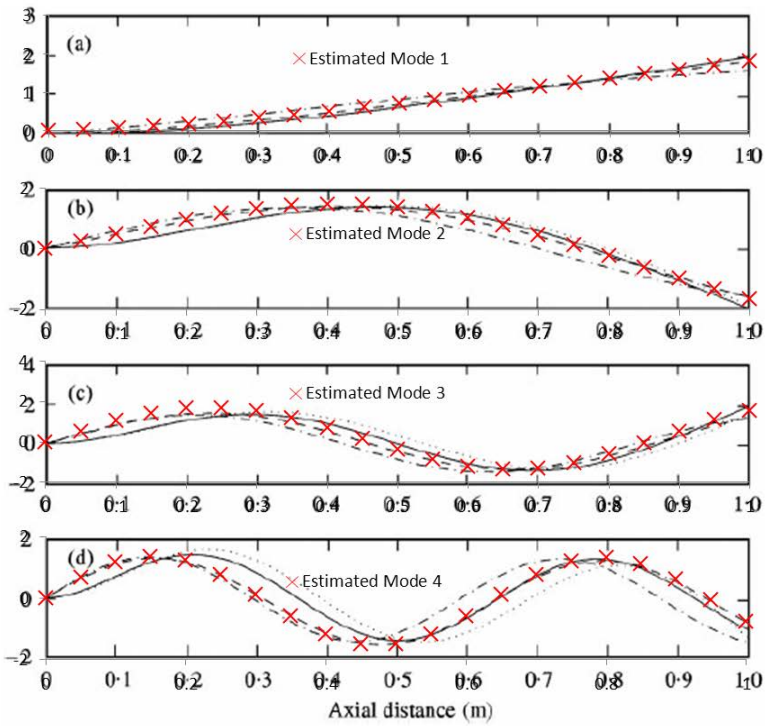

Figure 23. The first four mode shapes of the clamped–free beam: —, Euler–Bernoulli; ···, Rayleigh; –·–·–, shear; – – –, Timoshenko. (a) First mode, (b) second, (c) third, (d) fourth.

Fig. 6. Comparison of computed modal shapes for a fixed-free uniform steel tube in Han et al. [16].

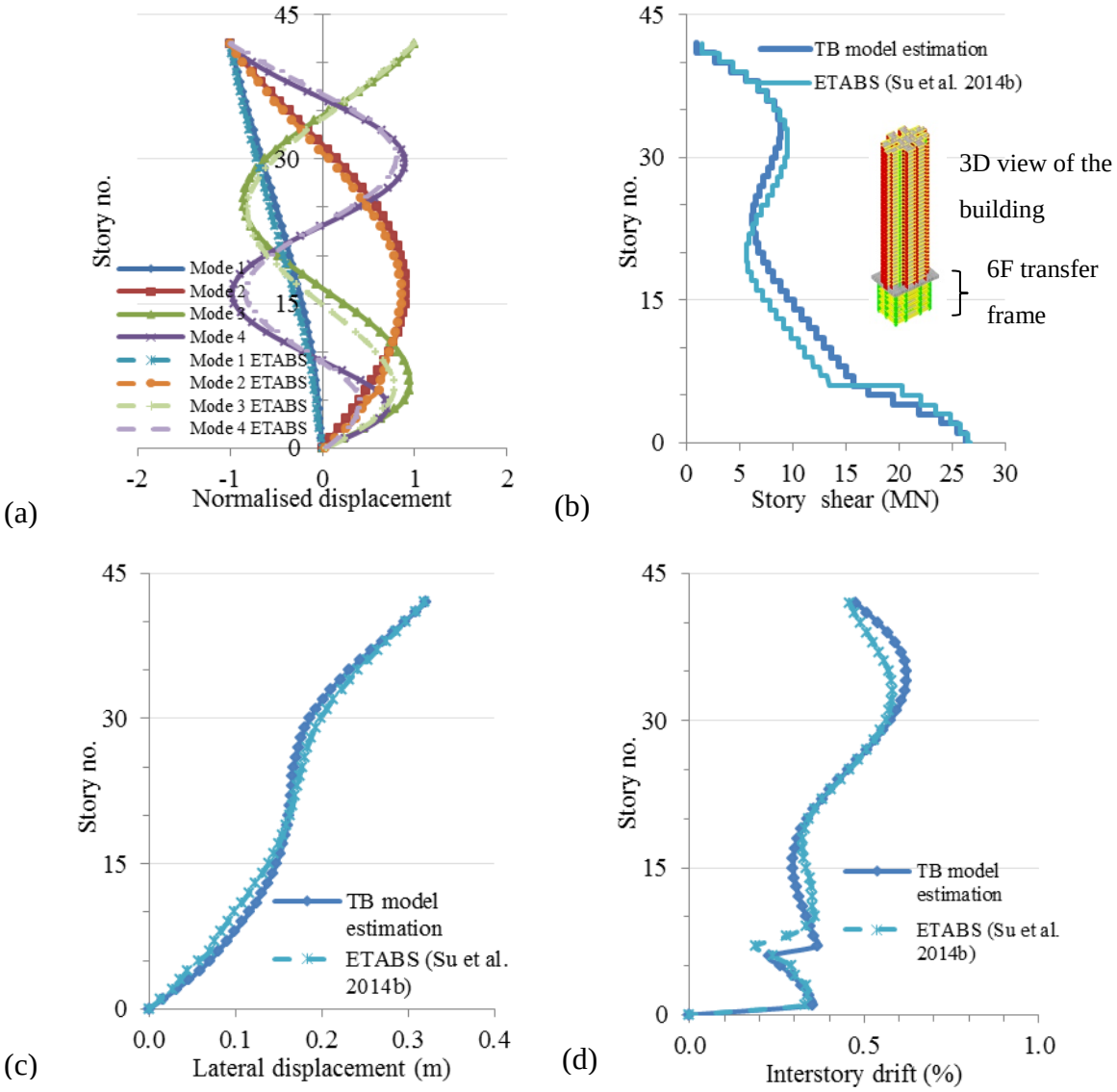

Fig. 7. Comparison of seismic demands from a full frame model by Su et al. [58] and a two-segment TB model for a typical RC residential building situated above a six story transfer structure: (a) modal shapes; (b) story shear, (c) story displacement and (d) inter-story drift subjected to a site-specific soil spectrum.

Estimated results from the two-segment TB model				
Mode	Period (sec)	Participating mass (%)	RSA(g)	Base shear (kN)
1	4.990	52.7	0.02	26303
2	1.558	26.9	0.23	
3	0.832	12.0	0.33	
4	0.575	3.5	0.33	
Results from ETABS model (by Su et al. [58])				
1	4.977	54.4	0.02	26651
2	1.446	25.1	0.26	
3	0.827	7.5	0.31	
4	0.511	1.0	0.27	

Table 3. Comparison of seismic demands in the typical residential building from Su et al. [58].

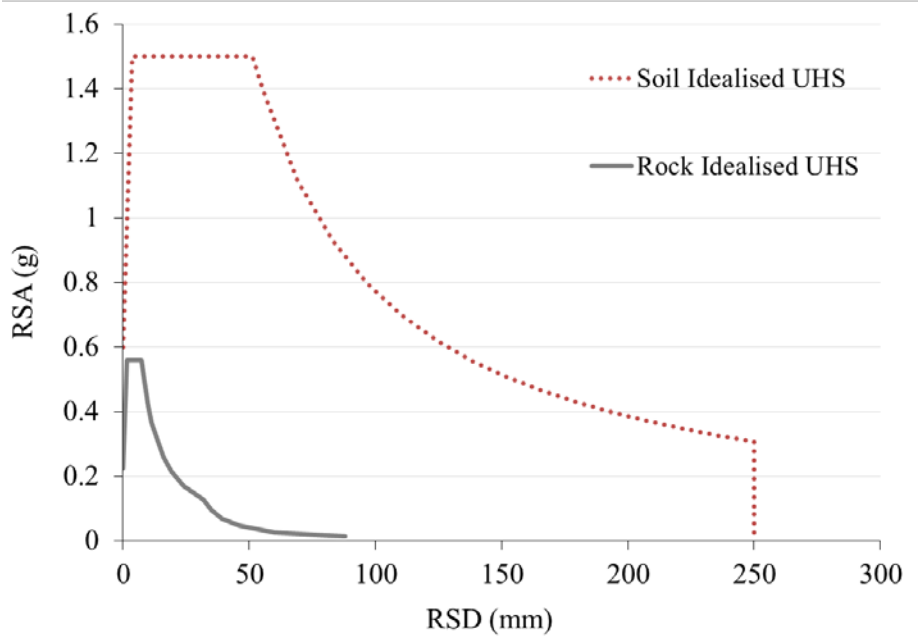

Fig. 8. Design spectrum of soil site for low-to-moderate seismicity region (Hong Kong, RP = 2475 years).

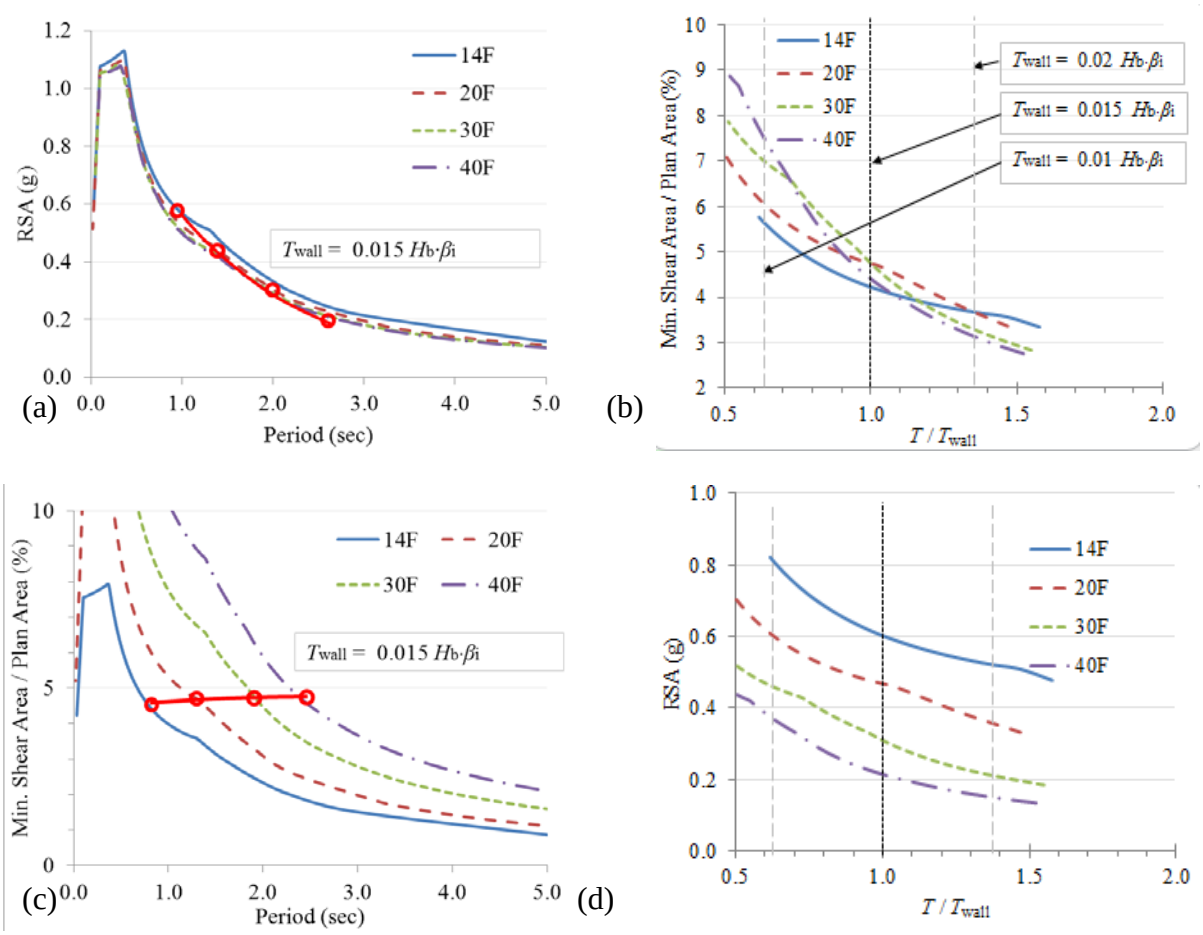

Fig. 9. Plot of (a) RSA against varied period; (b) normalized period; (c) minimum shear area ratio against varied period and (d) normalized period for medium- to high-rise buildings (assuming shear-to-flexural stiffness ratio r_{sf} = 10; β_i = 1.414; $\lambda_{T,R}$ = 1).

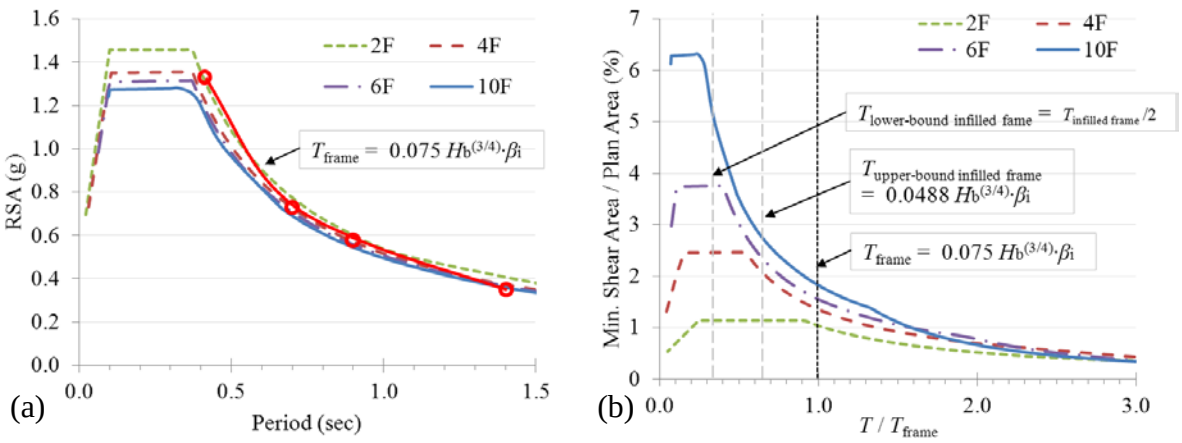

Fig. 10. Plot of (a) RSA against period and (b) minimum shear area ratio against normalized period for low-rise frame buildings (r_{sf} = 0.1).

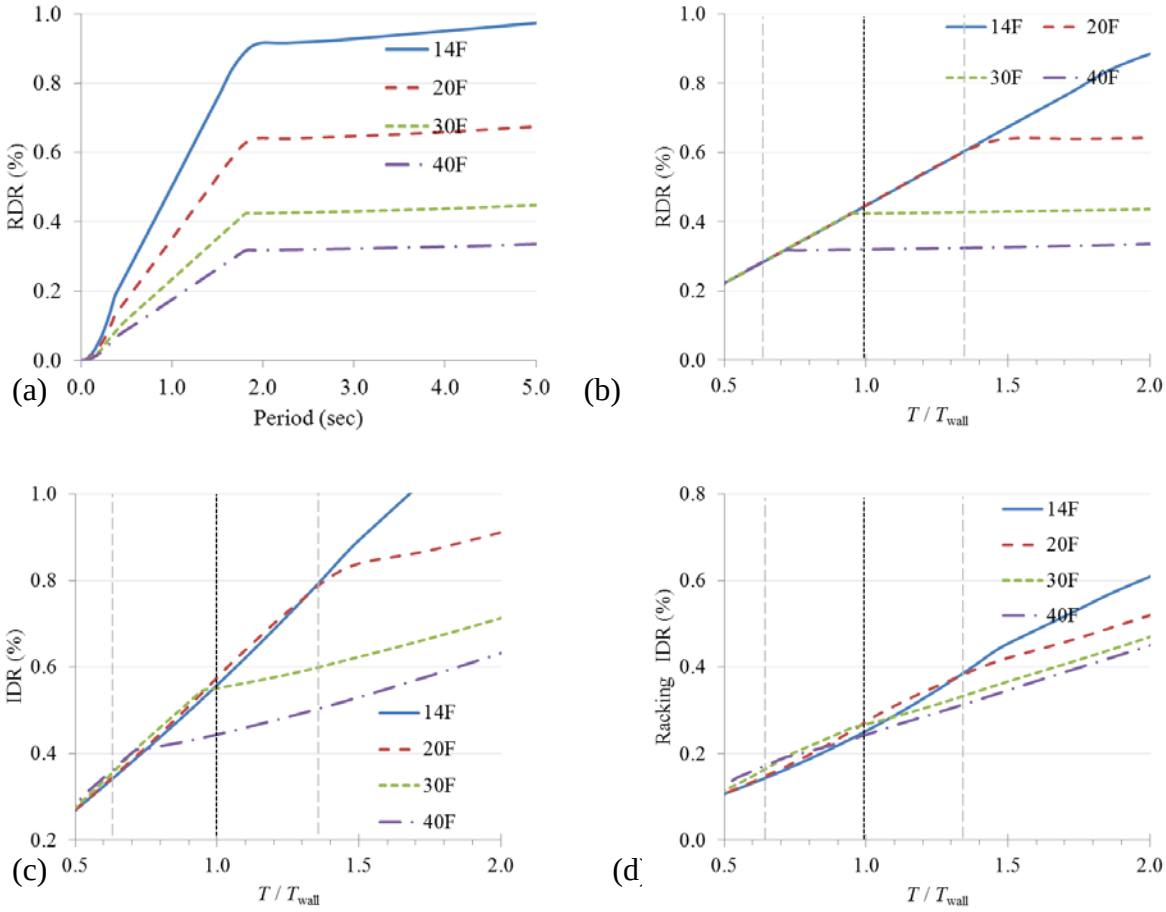

Fig. 11. Plot of roof (a) RDR against period; (b) RDR; (c) IDR and (d) racking IDR against normalized period for medium-to-high-rise buildings (r_{sf} = 10; β_i = 1.414; $\lambda_{T,Rd}$ = 1).

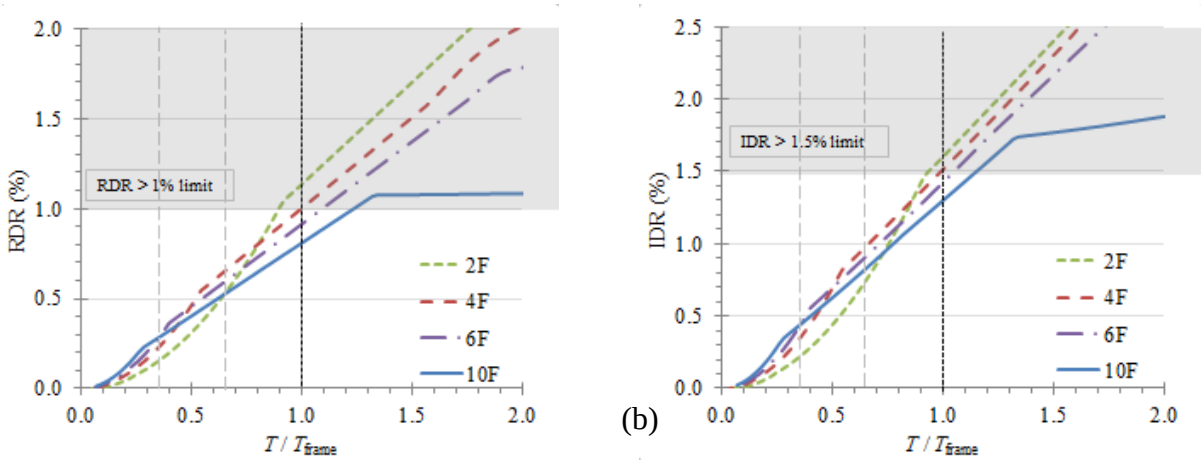

Fig. 12. Plot of (a) RDR and (b) IDR against normalized period for low-rise frame buildings (r_{sf} = 0.1; shaded regions indicate the limitations of the proposed analysis under large inelastic deformations).

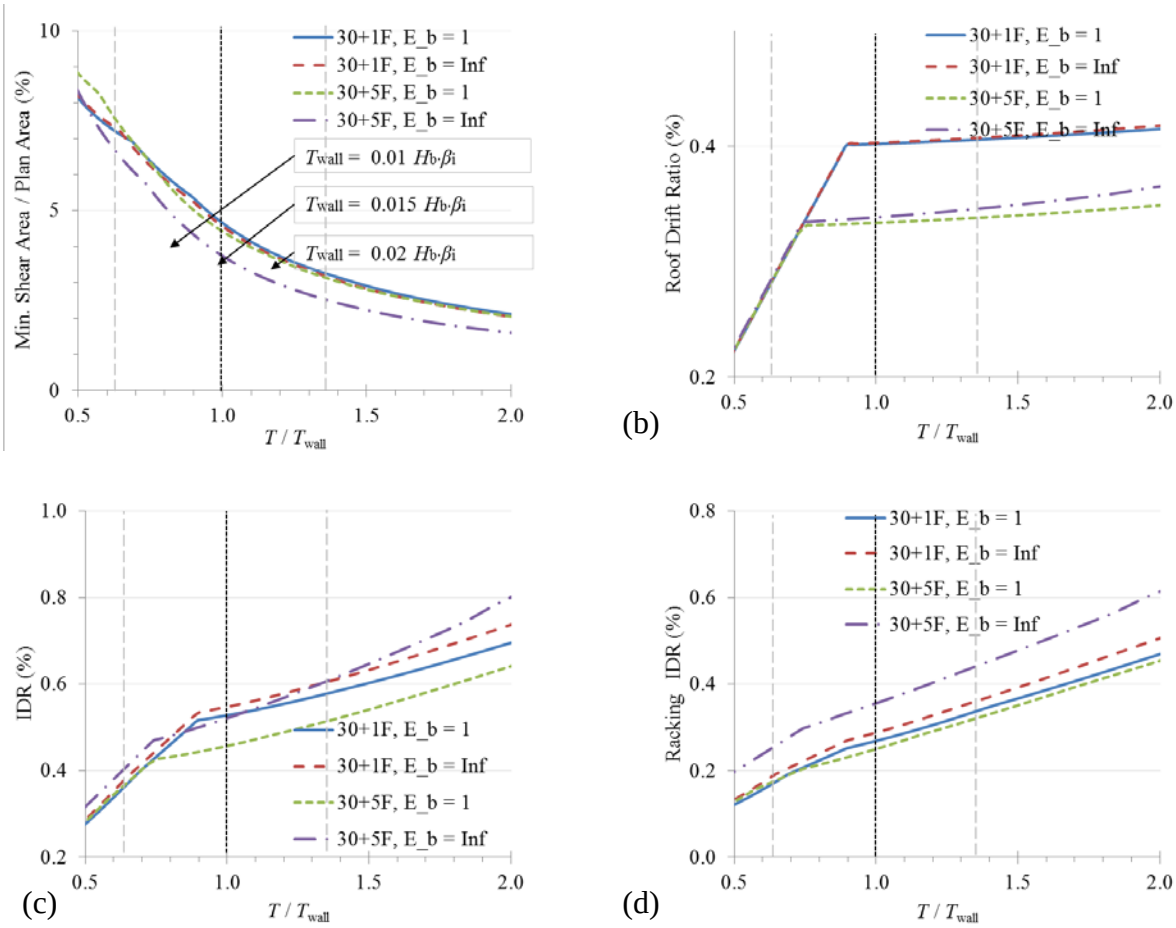

Fig. 13. Plot of (a) shear area ratio; (b) RDR; (c) IDR and (d) racking IDR against normalized period for high-rise transfer building (pseudo r_{sf} = 10; G_b = 1).

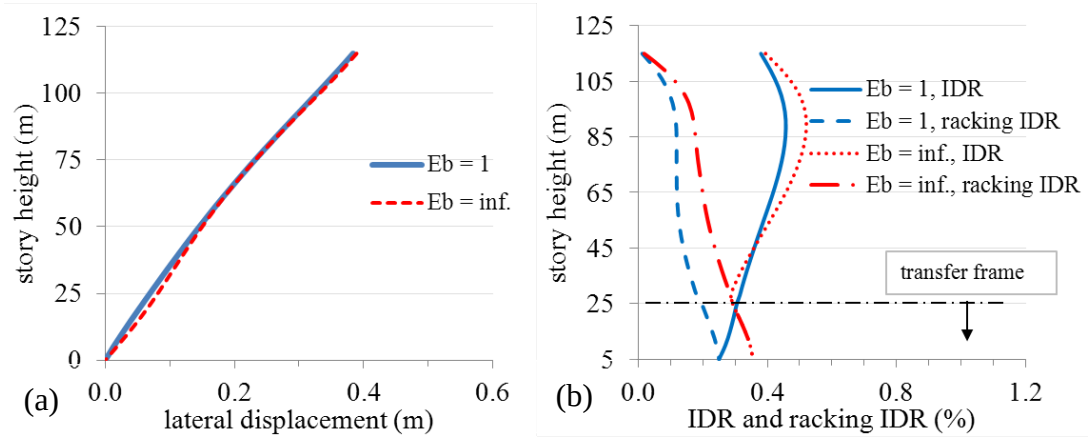

Fig. 14. Plot of (a) story displacement and (b) IDR and racking IDR against story height for high-rise transfer building (pseudo r_{sf} = 10; period = 2.43 sec; 30+5F TB model).

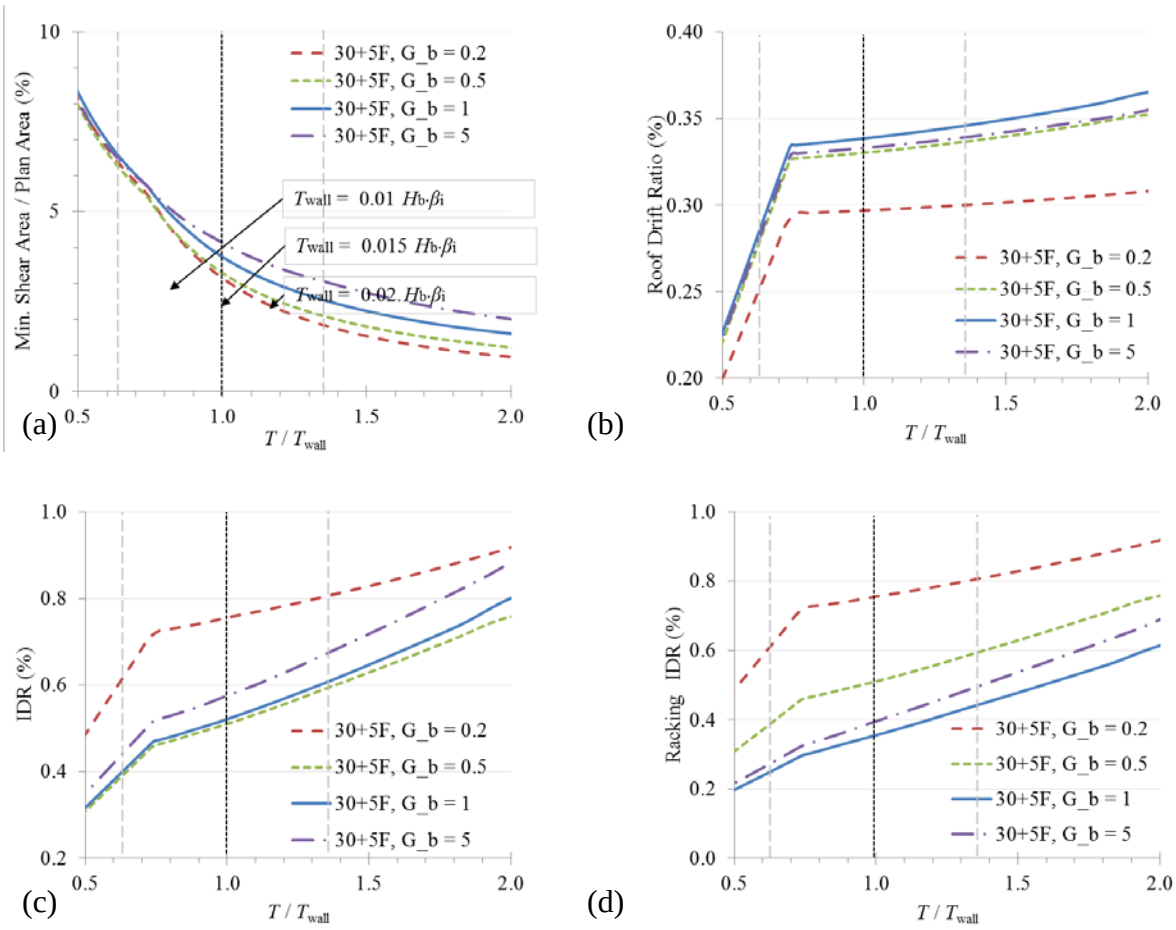

Fig. 15. Plot of (a) shear area ratio; (b) RDR; (c) IDR and (d) racking IDR against normalized period for high-rise transfer building (pseudo r_{sf} = 10; E_b = infinite).

Appendix A:

Formulation of non-uniform Timoshenko beam model with soil-structure interaction

The partial derivative of lateral deflection (w) of the Timoshenko beam (TB) model with respect to (w.r.t.) finite height ∂x yields the slope of the beam:

$$\frac{\partial w}{\partial x} = \Phi + \mu \tag{A1}$$

where Φ and γ_{xz} denote the rotation due to bending and the shear strain along the neutral axis, respectively, at the same cross section. From the strain-displacement relationship, the vertical axial strain ε_{xx} and shear strain γ_{xz} at the cross section are:

$$\varepsilon_{xx} = z\frac{\partial \Phi}{\partial x} \tag{A2}$$

$$\gamma_{xz} = -\Phi + \frac{\partial w}{\partial x} \tag{A3}$$

The strain energy (U) stored in the beam is:

$$U = \frac{1}{2}\int_0^L \int_A \sigma_{xx}\varepsilon_{xx} + \sigma_{xz}\gamma_{xz} dA dx \tag{A4}$$

where A denotes the cross sectional area of the beam, and σ_{xx} and σ_{xz} denote the corresponding axial and shear stress to the strains. Eq. (A2) and Eq. (A3) are substituted into Eq. (A4):

$$U = \frac{1}{2}\int_0^L \left[\frac{\partial \Phi}{\partial x}\int_A \sigma_{xx} z dA + (-\Phi + \frac{\partial w}{\partial x})\int_A \sigma_{xz} dA \right] dx \tag{A5}$$

$$U = \frac{1}{2}\int_0^L \left[\frac{\partial \Phi}{\partial x} M + (-\Phi + \frac{\partial w}{\partial x}) Q \right] dx \tag{A6}$$

where M and Q denote the moment and shear along the cross section respectively. Assuming free harmonic motion with rotary inertia, the kinematic energy T is equal to:

$$T = \frac{1}{2}\int_0^L \left[\rho A\omega^2 w^2 + \rho I\omega^2 \Phi^2\right] dx \tag{A7}$$

where ρ is the density (unit: ton/m^3) of the beam, and ω is the angular frequency of vibration. In accordance with the Hamilton's principle, the total energy of the system including external work done W_e conserves by any finite arbitrary perturbation in displacement (δw) and rotation ($\delta \Phi$) :

$$\delta(T - U) + \delta W_e = 0 \tag{A8}$$

$$\int_0^L \left[\rho A\omega^2 w\delta w + \rho I\omega^2 \Phi\delta\Phi\right] - \left[\frac{\partial\delta\Phi}{\partial x}M + (-\Phi + \frac{\partial\delta w}{\partial x})Q\right] dx = 0 \tag{A9}$$

where $W_e = 0$ under free vibration and integrating Eq. (A9) by parts result in:

$$\int_0^L \left[\left(\frac{\partial M}{\partial x} + Q + \rho I\omega^2\Phi\right)\delta\Phi + \left(\frac{\partial Q}{\partial x} + \rho A\omega^2 w\right)\delta w\right] dx - \left[M\delta\Phi\right]_0^L - \left[Q\delta w\right]_0^L = 0 \tag{A10}$$

Since δw and $\delta \Phi$ are arbitrary in 0 for $0 < x < L$ and the last two terms from Eq. (A10) can be eliminated under various BCs (e.g. fixed, hinge, sliding or free end), Eq. (A10) is valid only if:

$$\frac{\partial M}{\partial x} + Q + \rho I\omega^2\Phi = 0 \tag{A11}$$

$$\frac{\partial Q}{\partial x} + \rho A\omega^2 w = 0 \tag{A12}$$

From constitute relationships, the axial stress and shear stress are:

$$\sigma_{xx} = E\varepsilon_{xx} \tag{A13}$$

$$\sigma_{xz} = kG\gamma_{xz} \tag{A14}$$

where k = 2/3 accounts for the uneven stress distribution of the rectangular section and E and G denote the short-term Young's modulus and shear modulus of the material. By substituting Eq. (A2) and Eq. (A3) into the above equations and pre-multiplying Eq. (A13) by z, integration of the above equations along the sectional area A results in:

$$M = EI\frac{\partial \Phi}{\partial x} \tag{A15}$$

$$Q = kGA(-\Phi + \frac{\partial w}{\partial x}) \tag{A16}$$

Substituting the above equations into Eq. (A11) and (A12) yields:

$$EI\frac{\partial^2 \Phi}{\partial x^2} + kGA(-\Phi + \frac{\partial w}{\partial x}) + \rho I\omega^2 \Phi = 0 \tag{A17}$$

$$kGA(-\frac{\partial \Phi}{\partial x} + \frac{\partial^2 w}{\partial x^2}) + \rho A\omega^2 w = 0 \tag{A18}$$

assuming the harmonic motion, $w(x,t) = \overline{w}(x)e^{-i\omega t}$ and $\Phi(x,t) = \overline{\Phi}(x)e^{-i\omega t}$, where symbols within the parenthesis indicate the dependent variables which are omitted for brevity in the following. Hence, Eq. (A17) and Eq. (A18) can be expressed as:

$$EI\frac{\partial^2 \overline{\Phi}}{\partial x^2} + kGA(-\overline{\Phi} + \frac{\partial \overline{w}}{\partial x}) + \rho I\omega^2 \overline{\Phi} = 0 \tag{A19}$$

$$kGA(-\frac{\partial \overline{\Phi}}{\partial x} + \frac{\partial^2 \overline{w}}{\partial x^2}) + \rho A\omega^2 \overline{w} = 0 \tag{A20}$$

The above equations are rewritten in the terms of normalised $\tilde{x} = \left(\frac{x}{L}\right)$ and $\tilde{w} = \left(\frac{\overline{w}}{L}\right)$:

$$\Omega\frac{\partial^2\overline{\Phi}}{\partial\tilde{x}^2}+(-1+\frac{\lambda\Omega}{\xi})\overline{\Phi}+\frac{\partial\tilde{w}}{\partial\tilde{x}}=0 \tag{A21}$$

$$-\frac{\partial\overline{\Phi}}{\partial\tilde{x}}+\frac{\partial^2\tilde{w}}{\partial\tilde{x}^2}+\Omega\lambda\tilde{w}=0 \tag{A22}$$

where coefficient $\Omega=\frac{EI}{kGAL^2}$, $\lambda=\frac{\rho AL^4\omega^2}{EI}$ and $\xi=\frac{AL^2}{I}$. Decoupling of the above equations yields:

$$\frac{\partial^4\tilde{w}}{\partial\tilde{x}^4}+\lambda(\Omega+\frac{1}{\xi})\frac{\partial^2\tilde{w}}{\partial\tilde{x}^2}+\lambda(\frac{\lambda\Omega}{\xi}-1)\tilde{w}=0 \tag{A23}$$

$$\frac{\partial^4\overline{\Phi}}{\partial\tilde{x}^4}+\lambda(\Omega+\frac{1}{\xi})\frac{\partial^2\overline{\Phi}}{\partial\tilde{x}^2}+\lambda(\frac{\lambda\Omega}{\xi}-1)\overline{\Phi}=0 \tag{A24}$$

Since the above governing equations for $\overline{w}$ or $\overline{\Phi}$ are the same, by putting $\overline{w}$ or $\overline{\Phi}$ = $e^{n\tilde{x}}$, one can write:

$$n^4+\lambda(\Omega+\frac{1}{\xi})n^2+\lambda(\frac{\lambda\Omega}{\xi}-1)=0 \tag{A25}$$

$$n_{1,2,3,4}=\pm\sqrt{\frac{1}{2}\left[-\lambda\left(\Omega+\frac{1}{\xi}\right)\pm\sqrt{\lambda^2\left(\Omega+\frac{1}{\xi}\right)^2-4\lambda\left(\frac{\lambda\Omega}{\xi}-1\right)}\right]} \tag{A26}$$

The general solutions of $\overline{w}$ or $\overline{\Phi}$ are sub-divided into two regimes:

First regime for $\frac{\lambda\Omega}{\xi}<1$ (i.e. $\omega^2<\frac{kGA}{\rho I}$) or $f<f_c$ where $f_c=\frac{1}{2\pi}\sqrt{\frac{kGA}{\rho I}}$:

Since two n roots n_1 n_2 are always real, whereas another two roots n_3 and n_4 are always complex within the first regime, they can be simplified as a real root α and a complex root iβ. The general solution for $\overline{w}$ and $\overline{\Phi}$ are hyperbolic-trigonometric solutions:

$$\alpha = +\sqrt{\frac{1}{2}\left[-\lambda\left(\Omega+\frac{1}{\xi}\right)+\sqrt{\lambda^2\left(\Omega+\frac{1}{\xi}\right)^2-4\lambda\left(\frac{\lambda\Omega}{\xi}-1\right)}\right]} \qquad \epsilon \text{ real number} \quad \text{(A27)}$$

$$\beta = +\sqrt{\frac{1}{2}\left[+\lambda\left(\Omega+\frac{1}{\xi}\right)+\sqrt{\lambda^2\left(\Omega+\frac{1}{\xi}\right)^2-4\lambda\left(\frac{\lambda\Omega}{\xi}-1\right)}\right]} \qquad \epsilon \text{ real number} \quad \text{(A28)}$$

$$\tilde{w} = C_1\cosh(\alpha\tilde{x}) + C_2\sinh(\alpha\tilde{x}) + C_3\cos(\beta\tilde{x}) + C_4\sin(\beta\tilde{x}) \quad \text{(A29)}$$

$$\overline{\Phi} = D_1\sinh(\alpha\tilde{x}) + D_2\cosh(\alpha\tilde{x}) + D_3\sin(\beta\tilde{x}) + D_4\cos(\beta\tilde{x}) \quad \text{(A30)}$$

The coefficients D_i could be expressed in terms of C_i by substituting the above equations into either Eq. (A21) or Eq. (A22):

$$D_1 = \frac{\alpha^2+\lambda\Omega}{\alpha}C_1 = \Psi_\alpha C_1; \quad D_2 = \frac{\alpha^2+\lambda\Omega}{\alpha}C_2 = \Psi_\alpha C_2;$$
$$D_3 = \frac{-\beta^2+\lambda\Omega}{\beta}C_3 = \Psi_\beta C_3; \; D_4 = \frac{\beta^2-\lambda\Omega}{\beta}C_4 = -\Psi_\beta C_3 \quad \text{(A31)}$$

where coefficient $\Psi_\alpha = \frac{-\alpha^2+\lambda\Omega}{\alpha}$ and $\Psi_\beta = \frac{-\beta^2+\lambda\Omega}{\beta}$.

Second regime for $\frac{\lambda\Omega}{\xi} > 1$ (i.e. $\omega^2 > \frac{kGA}{\rho I}$) or $f > f_c$:

Since four n roots $n_{1,2,3,4}$ are always complex within the second regime, they can be simplified as a complex root iα and a complex root iβ. The general solution for $\tilde{w}$ and $\overline{\Phi}$ are trigonometric solutions:

$$\alpha = +\sqrt{\frac{1}{2}\left[+\lambda\left(\Omega+\frac{1}{\xi}\right)-\sqrt{\lambda^2\left(\Omega+\frac{1}{\xi}\right)^2-4\lambda\left(\frac{\lambda\Omega}{\xi}-1\right)}\right]} \qquad \epsilon \text{ real number} \quad \text{(A32)}$$

$$\beta = +\sqrt{\frac{1}{2}\left[+\lambda\left(\Omega+\frac{1}{\xi}\right)+\sqrt{\lambda^2\left(\Omega+\frac{1}{\xi}\right)^2-4\lambda\left(\frac{\lambda\Omega}{\xi}-1\right)}\right]} \qquad \epsilon \text{ real number} \quad \text{(A33)}$$

$$\tilde{w} = C_1\cos(\alpha\tilde{x}) + C_2\sin(\alpha\tilde{x}) + C_3\cos(\beta\tilde{x}) + C_4\sin(\beta\tilde{x}) \quad \text{(A34)}$$

$$\overline{\Phi} = D_1 \sin(\alpha\tilde{x}) + D_2 \cos(\alpha\tilde{x}) + D_3 \sin(\beta\tilde{x}) + D_4 \cos(\beta\tilde{x}) \tag{A35}$$

The coefficients D_i could be expressed in terms of C_i by substituting the above equations into either Eq. (A21) or Eq. (A22):

$$\begin{aligned} D_1 &= \frac{-\alpha^2 + \lambda\Omega}{\alpha} C_1 = \Psi_\alpha C_1; \quad D_2 = \frac{\alpha^2 - \lambda\Omega}{\alpha} C_2 = -\Psi_\alpha C_2 \ ; \\ D_3 &= \frac{-\beta^2 + \lambda\Omega}{\beta} C_3 = \Psi_\beta C_3; \quad D_4 = \frac{\beta^2 - \lambda\Omega}{\beta} C_4 = -\Psi_\beta C_3 \end{aligned} \tag{A36}$$

where the coefficient $\Psi_\alpha = \frac{-\alpha^2 + \lambda\Omega}{\alpha}$ and $\Psi_\beta = \frac{-\beta^2 + \lambda\Omega}{\beta}$. The rotational symmetry between α and β can be observed in this solution.

The governing equations are determined from the boundary conditions. For a cantilever TB supported on a soil spring [12,19], the moment and lateral force equilibrium are satisfied at the base ($\tilde{x}$ = 0) and zero moment and lateral load are applied at the top ($\tilde{x}$ = 1):

$$kGA(-\overline{\Phi} + \frac{\partial\tilde{w}}{\partial\tilde{x}}) - K_T \tilde{w} L = 0 \qquad \text{at} \quad \tilde{x} = 0 \tag{A37a}$$

$$\frac{EI}{L}(\frac{\partial\overline{\Phi}}{\partial\tilde{x}}) - K_R \overline{\Phi} = 0 \qquad \text{at} \quad \tilde{x} = 0 \tag{A37b}$$

$$\frac{M}{EI} = \frac{1}{L}\frac{\partial\overline{\Phi}}{\partial\tilde{x}} = 0 \qquad \text{at} \quad \tilde{x} = 1 \tag{A37c}$$

$$\frac{Q}{kGA} = \gamma_{xz} = \frac{\partial\tilde{w}}{\partial\tilde{x}} - \overline{\Phi} = 0 \qquad \text{at} \quad \tilde{x} = 1 \tag{A37d}$$

where K_T and K_R denote the translational and rotational stiffnesses by the soil respectively. Detailed conversion from foundation soil properties to K_T and K_R may refer to Cheng and Heaton [12]. If K_T and K_R tend to infinite, the BC for Eq. (A37a) and Eq. (A37b) reduce to the fixed end BCs: $\overline{w}$ = 0 and $\overline{\Phi}$ = 0 at the base ($\tilde{x}$ = 0).

For vibration mode within the first regime ($f < f_c$), substituting Eqs. (A27 to A31) into the BCs in Eq. (A37) results in a system of equations:

$$\begin{bmatrix} -K_T L, & kGA(-\Psi_\alpha + \alpha), & -K_T L, & kGA(\Psi_\beta + \beta) \\ \frac{EI}{L}\Psi_\alpha \alpha, & -K_R \Psi_\alpha, & \frac{EI}{L}\Psi_\beta \beta, & K_R \Psi_\beta \\ \Psi_\alpha \alpha \cosh(\alpha), & \Psi_\alpha \alpha \sinh(\alpha), & \Psi_\beta \beta \cos(\beta), & \Psi_\beta \beta \sin(\beta) \\ (\alpha - \Psi_\alpha)\sinh(\alpha), & (\alpha - \Psi_\alpha)\cosh(\alpha), & -(\beta + \Psi_\beta)\sin(\beta), & (\beta + \Psi_\beta)\cos(\beta) \end{bmatrix} \cdot \begin{pmatrix} C_1 \\ C_2 \\ C_3 \\ C_4 \end{pmatrix} = \begin{pmatrix} 0 \\ 0 \\ 0 \\ 0 \end{pmatrix} \tag{A38}$$

For the vibration mode lying in the second regime ($f > f_c$), it becomes:

$$\begin{bmatrix} -K_T L, & kGA(\Psi_\alpha + \alpha), & -K_T L, & kGA(\Psi_\beta + \beta) \\ \frac{EI}{L}\Psi_\alpha \alpha, & K_R \Psi_\alpha, & \frac{EI}{L}\Psi_\beta \beta, & K_R \Psi_\beta \\ \Psi_\alpha \alpha \cos(\alpha), & \Psi_\alpha \alpha \sin(\alpha), & \Psi_\beta \beta \cos(\beta), & \Psi_\beta \beta \sin(\beta) \\ -(\alpha + \Psi_\alpha)\sin(\alpha), & (\alpha + \Psi_\alpha)\cos(\alpha), & -(\beta + \Psi_\beta)\sin(\beta), & (\beta + \Psi_\beta)\cos(\beta) \end{bmatrix} \cdot \begin{pmatrix} C_1 \\ C_2 \\ C_3 \\ C_4 \end{pmatrix} = \begin{pmatrix} 0 \\ 0 \\ 0 \\ 0 \end{pmatrix} \tag{A39}$$

By solving the characteristic equations in Eq. (A38) or Eq. (A39), the eigen-frequencies (f) of a particular mode can be determined. Thus, C_i can be determined by substituting f into the characteristic equations. Corresponding modal shapes can then be derived from Eqs. (A29 to A30) or Eqs. (A34 to A35). The above derivations present the solutions for a single uniform prismatic Timoshenko beam; in the case of a two-segment TB model, the derivations are similar:

In the first regime ($f > f_c$), the general solution remains similar. Only the structural properties are defined by the bottom beam comprising the shear stiffness G_1A_1, flexural stiffness E_1I_1, and bottom beam height H_1. For $0 \le x \le H$:

$$\tilde{w}_1 = C_{11}\cosh(\alpha_1 \tilde{x}_1) + C_{21}\sinh(\alpha_1 \tilde{x}_1) + C_{31}\cos(\beta_1 \tilde{x}_1) + C_{41}\sin(\beta_1 \tilde{x}_1) \tag{A40}$$

$$\overline{\Phi}_1 = D_{11}\sinh(\alpha_1 \tilde{x}_1) + D_{21}\cosh(\alpha_1 \tilde{x}_1) + D_{31}\sin(\beta_1 \tilde{x}_1) + D_{41}\cos(\beta_1 \tilde{x}_1) \tag{A41}$$

where $\tilde{x}_1 = x/H_1$, $\tilde{w}_1 = w/H_1$, and additional subscript 1 denotes the properties corresponding to the bottom beam. Similarly the general solution for the upper beam

when $H_1 \le x \le H_1 + H_2$ is:

$$\tilde{w}_2 = C_{12}\cosh(\alpha_2\tilde{x}_2) + C_{22}\sinh(\alpha_2\tilde{x}_2) + C_{32}\cos(\beta_2\tilde{x}_2) + C_{42}\sin(\beta_2\tilde{x}_2) \quad \text{(A42)}$$

$$\overline{\Phi}_2 = D_{12}\sinh(\alpha_2\tilde{x}_2) + D_{22}\cosh(\alpha_2\tilde{x}_2) + D_{32}\sin(\beta_2\tilde{x}_2) + D_{42}\cos(\beta_2\tilde{x}_2) \quad \text{(A43)}$$

where $\tilde{x}_2 = (x\text{-}H_1)/H_2$, $\tilde{w}_2 = w/H_2$, and additional subscript 2 denotes the properties corresponding to the upper beam.

The BCs in Eq. (37) at the base of the bottom beam ($\tilde{x}_1 = 0$) and top of the upper beam ($\tilde{x}_2 = 1$) remain unchanged. Four additional BCs at the adjoining node ($\tilde{x}_1 = 1$ or $\tilde{x}_2 = 0$) between the two beams involve (a) the continuous lateral displacement ($w_1 = w_2$), (b) the continuous rotation ($\overline{\Phi}_1 = \overline{\Phi}_2$), (c) shear force equilibrium and (d) the moment equilibrium:

$$H_1\tilde{w}_1 = H_2\tilde{w}_2 \quad \text{at} \quad \tilde{x}_1 = 1,\ \tilde{x}_2 = 0 \quad \text{(A44a)}$$

$$\overline{\Phi}_1 = \overline{\Phi}_2 \quad \text{at} \quad \tilde{x}_1 = 1,\ \tilde{x}_2 = 0 \quad \text{(A44b)}$$

$$k_1G_1A_1\left(-\overline{\Phi}_1 + \frac{\partial\tilde{w}_1}{\partial\tilde{x}_1}\right) = k_2G_2A_2\left(-\overline{\Phi}_2 + \frac{\partial\tilde{w}_2}{\partial\tilde{x}_2}\right) \quad \text{at} \quad \tilde{x}_1 = 1,\ \tilde{x}_2 = 0 \quad \text{(A44c)}$$

$$\frac{E_1I_1}{H_1}\frac{\partial\overline{\Phi}_1}{\partial\tilde{x}_1} = \frac{E_2I_2}{H_2}\frac{\partial\overline{\Phi}_2}{\partial\tilde{x}_2} \quad \text{at} \quad \tilde{x}_1 = 1,\ \tilde{x}_2 = 0 \quad \text{(A44d)}$$

Hence, the system of equation is revised to:

$$\begin{bmatrix} -K_T H_{1,} & k_1 G_1 A_1(-\Psi_{\alpha 1}+\alpha_1), & -K_T H_{1,} & k_1 G_1 A_1(\Psi_{\beta 1}+\beta_1), & \dots \\ \frac{E_1 I_1}{H_1}\Psi_{\alpha 1}\alpha_1, & -K_R\Psi_{\alpha 1}, & \frac{E_1 I_1}{H_1}\Psi_{\beta 1}\beta_1, & K_R\Psi_{\beta 1}, & \dots \\ 0, & 0, & 0, & 0, & \dots \\ 0, & 0, & 0, & 0, & \dots \\ \cosh(\alpha_1), & \sinh(\alpha_1), & \cos(\beta_1), & \sin(\beta_1), & \dots \\ \Psi_{\alpha 1}\sinh(\alpha_1), & \Psi_{\alpha 1}\cosh(\alpha_1), & \Psi_{\beta 1}\sin(\beta_1), & -\Psi_{\beta 1}\cos(\beta_1), & \dots \\ (\alpha_1-\Psi_{\alpha 1})\sinh(\alpha_1), & (\alpha_1-\Psi_{\alpha 1})\cosh(\alpha_1), & -(\beta_1+\Psi_{\beta 1})\sin(\beta_1), & (\beta_1+\Psi_{\beta 1})\cos(\beta_1), & \dots \\ \Psi_{\alpha 1}\alpha_1\cosh(\alpha_1), & \Psi_{\alpha 1}\alpha_1\sinh(\alpha_1), & \Psi_{\beta 1}\beta_1\cos(\beta_1), & \Psi_{\beta 1}\beta_1\sin(\beta_1), & \dots \end{bmatrix}$$

$$\begin{bmatrix} \dots & 0, & 0, & 0, & 0 \\ \dots & 0, & 0, & 0, & 0, \\ \dots & \Psi_{\alpha 2}\alpha_2\cosh(\alpha_2), & \Psi_{\alpha 2}\alpha_2\sinh(\alpha_2), & \Psi_{\beta 2}\beta_2\cos(\beta_2), & \Psi_{\beta 2}\beta_2\sin(\beta_2) \\ \dots & (\alpha_2-\Psi_{\alpha 2})\sinh(\alpha_2), & (\alpha_2-\Psi_{\alpha 2})\cosh(\alpha_2), & -(\beta_2+\Psi_{\beta 2})\sin(\beta_2), & (\beta_2+\Psi_{\beta 2})\cos(\beta_2) \\ \dots & -c_h, & 0, & -c_h, & 0 \\ \dots & 0, & -\Psi_{\alpha 2}, & 0, & \Psi_{\beta 2} \\ \dots & 0, & -c_g(\alpha_2-\Psi_{\alpha 2}), & 0, & -c_g(\beta_2+\Psi_{\beta 2}) \\ \dots & -\frac{c_k}{c_h}\Psi_{\alpha 2}\alpha_2, & 0, & -\frac{c_k}{c_h}\Psi_{\beta 2}\beta_2, & 0 \end{bmatrix}_{8\times 8} \cdot \begin{pmatrix} C_{11} \\ C_{21} \\ C_{31} \\ C_{41} \\ C_{12} \\ C_{22} \\ C_{32} \\ C_{42} \end{pmatrix} = \begin{pmatrix} 0 \\ 0 \\ 0 \\ 0 \\ 0 \\ 0 \\ 0 \\ 0 \end{pmatrix}$$

(A45)

where c_h, c_k and c_g denote the relative height (= H_2/H_1), flexural stiffness (= E_2I_2/E_1I_1) and shear stiffness (= $k_2G_2A_2/k_1G_1A_1$) respectively.

On the arising of the second regime, there are three possible cases: (1) $f > f_{c1}$ bottom beam critical frequency; (2) $f > f_{c2}$ upper beam critical frequency and (3) $f > f_{c1}$ and f_{c2}. The solutions vary slightly from (A45) by replacing the corresponding Eq. in (A40 to A43) with trigonometric form as in Eq. (A34) and Eq. (A35). Similar derivations are not repeated here.